Dynamic MRI: Techniques and Applications

A Dissertation

Presented to

the faculty of the School of Engineering and Applied Science

University of Virginia

---

in partial fulfillment

of the requirements for the degree

Doctor of Philosophy

by

Xue Feng

August

2012

APPROVAL SHEET

The dissertation

is submitted in partial fulfillment of the requirements

for the degree of

Doctor of Philosophy

AUTHOR

The dissertation has been read and approved by the examining committee:

Advisor

Accepted for the School of Engineering and Applied Science:

Dean, School of Engineering and Applied Science

August

2012

Abstract

Spiral k-space MRI is a fast imaging technique that uses a spiral acquisition pattern to cover more k-space area during each repetition time to reduce the number of excitations required to cover k-space. It is also robust to flow and motion artifacts because the center of k-space is repeatedly scanned and the gradient moments are not accumulating. Therefore, spiral scanning is a good choice for many dynamic applications. However, the non-Cartesian sampling pattern makes it more susceptible to off-resonance effects, k-space trajectory infidelity and density compensation function (DCF) estimation errors and thus corrections are required to avoid image degradation.

Balanced steady-state free precession (bSSFP) sequences are widely used in real-time cardiac MRI, because of their short acquisition time and high contrast between the blood pool and myocardium. Non-Cartesian bSSFP sequences represented by radial and spiral play an important role in this application due to their reduced scan time. However, the refocusing mechanism with TE=TR/2 in a typical bSSFP sequence is not realized with the traditional spiral-out bSSFP sequence. Therefore, we sought to develop a new spiral-in/out bSSFP sequence

to move TE to the center of TR. The ultimate goal of this study is to implement the radial, spiral-out and spiral-in/out bSSFP sequences and compare their performances in real-time cardiac function MRI. The two spiral bSSFP sequences show reduced aliasing and improved image quality from blind review. In addition, the refocusing mechanism of the spiral-in/out bSSFP improves the SNR and can be used for reliable fat-water separation.

Real-time velum imaging during speech is a new dynamic MRI application which can be used for diagnosis of velopharyngeal insufficiency (VPI) and velum muscle modeling. A spiral gradient-recalled-echo (GRE) sequence can be used in this application for faster data acquisition. However, the requirements for spatial and temporal resolution and SNR are so demanding that spiral parallel imaging techniques are also required to further reduce the scan time. In addition, the off-resonance effect due to air-tissue boundary needs to be corrected to deblur the dynamic image series. Spiral spatial and temporal parallel imaging techniques and off-resonance correction focusing on this application are explored to realize $1.1 * 1.1$ mm^2 spatial resolution, 20 fps temporal resolution and simultaneous two-slice coverage with 6x undersampling. The sequence and the protocol for this application were developed and tested. The study demonstrates the potential applicability of these techniques in VPI diagnosis and velum muscle modeling.

Even though spiral scanning is an important alternative method, the Cartesian trajectory is still clinically dominant. In Cartesian dynamic MRI, spatial and temporal parallel imaging can be exploited to reduce scan time. Real-time reconstruction enables immediate visualization during the scan. Commonly used view-sharing techniques suffer from limited temporal resolution, and many of the more advanced reconstruction methods are either retrospective, time-consuming, or both. A Kalman filter model capable of real-time reconstruction can be used to increase the spatial and temporal resolution in dynamic MRI reconstruction. The original study describing the use of the Kalman filter in dynamic MRI was limited to non-Cartesian trajectories, because of a limitation intrinsic to the dynamic model used in that study. Here the limitation is overcome and the model is applied to the more commonly used Cartesian trajectory with fast reconstruction. Furthermore, a combination of the Kalman filter model with Cartesian parallel imaging is presented to further increase the spatial and temporal resolution and SNR. Simulations and experiments were conducted to demonstrate that the Kalman filter model can increase the temporal resolution of the image series compared with view sharing techniques and decrease the spatial aliasing compared with TGRAPPA. The method requires relatively little computation, and thus is suitable for real-time reconstruction.

Acknowledement

I still remember the day when I first went to Dr. Craig Meyer's office to discuss my future and MRI research. When I went out, I made a decision that I should follow this professor to do MRI research for the next few years. This has proved to be one of the most important and wisest decisions I have made in my life. I owe my deepest gratitude to my advisor, Dr. Craig Meyer, because he is the one who introduced me to MRI research. During the past five years, he not only taught me numerous aspects of MRI and guided me in the research with his knowledge and witness, but also influenced my attitude towards research with his enthusiasm and confidence. I feel lucky to have such a wonderful person to guide me in my life.

I have to admit that these same words were used two years ago to express my gratitude for him in my Master thesis. When I look back and read them again, I did not feel any less gratitude all through these years. In fact, my gratitude continues growing with all the personal care I received from him both on research and career development. No words can fully represent it. Saying these words twice is not enough either.

Next I would like to thank Dr. Michael Salerno for serving on my committee and his enormous help on my research. Our talks on various research topics are very enlightening for me. Besides, it has always been a pleasure to talk to him thanks to his patience and humor. I really enjoyed working with him during the past few years.

I would also thank Dr. Christopher Kramer for all the help on the research. He and Dr. Michael Salerno reviewed all the cardiac images in my study and provided a lot of valuable information. MRI research becomes much more valuable when it is applied to improve actual patient care and it is impossible without their help as cardiologists. In addition, thanks for the pool party every summer. I will definitely miss it if I leave Charlottesville in the future.

I also would like to thank Dr. Silvia Blemker. The dynamic velum imaging project she brought to us is really interesting and promising. More importantly, the experience of working together with people from different areas I gained with this project is very valuable. I feel regretful for not being able to finish this project with her and other researchers but I will provide all the available assistance if needed.

I would also thank Dr. Frederick Epstein and Dr. John Mugler for serving on my committee and providing valuable suggestions on my research. I feel grateful to finish my PhD research in this place with so many distinguished professors, including them, since I can always learn a lot from them. I want to express my special gratitude to Dr. Frederick Epstein for being my chair at the last minute when Dr. John Hossack was unable to attend my defense. Meanwhile, I also give my thanks to Dr. John Hossack for all the previous work on chairing my committee. It is very unfortunate for me to not have him continue to serve on my committee due to the schedule conflict.

I also give my thanks to Dr. Hao Tan, Dr. Weitian Chen and Dr. Christopher Sica for their help when I first started MRI research. It would take much more time for me to understand many MRI principles and get familiar with programming the MR scanner without their help.

I also thank Dr. Brian Hargreaves, Dr. James Pipe and Dr. Joelle Barral for the help in my career development.

I would also thank my colleagues: Samuel Fielden, Meihan Wang, Qingfeng Mao, Li Zhao, Yang Yang, Xiao Chen, Kun Qing and Dr. Ken Johnson. I do not remember how many times we discussed and got excited with new findings. It has been a great pleasure to work with them.

Finally, I would like to thank my parents for their support. More importantly, I would thank my fiancee Yu Cao for everything she has done for me. I cannot imagine one single day without her. I dedicate the dissertation to them and looking forward to having a wonderful wedding soon.

Contents

List of Figures

Chapter 1

Introduction

Magnetic resonance imaging (MRI) is a powerful noninvasive and nonradioactive imaging technique that has experienced rapid growth over the past several decades. The main advantages of MRI compared to other major imaging modalities such as computed tomography (CT) and ultrasound include excellent soft tissue contrast and flexibility in generating image contrast and selecting imaging parameters for control of image content. The main disadvantage, on the other hand, is the relatively low imaging speed. However, recent development of MRI hardware and various fast imaging techniques aiming to reduce scan time have greatly alleviated this disadvantage; therefore, many clinical imaging applications in which a series of dynamic MR images are rapidly acquired to capture evolving physiological phenomena have become plausible and also have attracted more and more research attention. These applications including real-time cardiac function MRI, dynamic myocardial perfusion imaging, real-time MR speech imaging, time-resolved magnetic resonance angiography (MRA), and dynamic functional MRI.

Among the various fast imaging techniques, spiral k-space MRI [1, 2] is an important method drawing much attention. It uses a spiral acquisition pattern to cover more k-space area during each repetition time (TR) and therefore greatly reduces the number of excitations required to cover the entire k-space. In addition to the high data acquisition efficiency, spiral scanning is more robust to flow and motion artifacts because the center of k-space is repeatedly scanned and the gradient moments are not accumulating. Therefore, spiral scanning is a good choice for many dynamic applications.

However, the non-Cartesian sampling pattern of the spiral trajectories makes it more susceptible to many imperfections of the system. For example, B_0 field inhomogeneity and concomitant gradient fields can lead to off-resonance effects, resulting in severe image blurring and/or distortion, especially when the spiral readout time is relatively long. In addition, eddy-current effects are more conspicuous for spiral trajectories as the gradients and the slew rates are constantly changing during the acquisition. The anisotropic delay on three gradient axes and the linear eddy currents can cause the actual k-space trajectory to deviate from the theoretical trajectory and bring in blurring and distortions in the reconstructed images [3]. Many methods have been developed to correct for these effects, including advanced shimming tools to reduce B_0 field inhomogeneity [4], automatic eddy current compensation in the gradient system [5, 6] and various post processing algorithms during the image reconstruction. In addition to these correction algorithms in spiral image reconstruction, the density compensation factor (DCF) also plays an important role as it not only affects the accuracy of transforming the non-Cartesian k-space data onto Cartesian grids but also can perform as a raw data filter for a specific purpose [7–9]. Therefore, before we explore the dynamic applications using the spiral trajectories, we will introduce the general correction algorithms including off-resonance and trajectory infidelity corrections and the DCF calculation method. However, even though these methods have proved their effectiveness with static spiral image acquisition, special considerations are still required for different dynamic applications.

1.1 Specific Aims

After introducing these general techniques in spiral reconstruction, we will focus on three specific aims for this dissertation to describe different techniques and applications in dynamic MRI.

Real-time cardiac function MRI has proved to be clinically useful for evaluating cardiac function, visualizing cardiac flow, and localizing scan plans for coronary imaging [11–13]. For this application, balanced steady-state free precession (bSSFP, also known as True-FISP, FIESTA, or balanced FFE) [14, 15] sequences are widely used because of their short acquisition time and high contrast between blood pool and myocardium. Non-Cartesian sampling patterns represented by radial and the aforementioned spiral trajectories are generally more time-efficient than a Cartesian sampling pattern that fills k-space line by line. Therefore, non-Cartesian bSSFP sequences [16, 17] play an important role in real-time cardiac function imaging. Nevertheless, radial bSSFP and spiral bSSFP have different mechanisms to reduce scan time and perform differently in this application. In addition, in a typical bSSFP sequence, the echo time (TE) is usually at the center of TR to exploit the refocusing effect similar to a spin echo [15], which is not true for traditional spiral bSSFP sequences, where the k-space scanning starts at the center and moves to the edge in a spiral path. Therefore, we want to develop a spiral-in/out bSSFP sequence to move TE to the center of TR. With respect to the new spiral-in/out bSSFP sequence, the traditional bSSFP sequence is renamed as spiral-out bSSFP sequence. For this dissertation, **Specific Aim #1 is to implement all three bSSFP sequences (radial, spiral/out and spiral-in/out) on the scanner and compare their performance in real-time cardiac function MRI.** For the comparison, in addition to theoretical analysis of the point spread functions (PSF), we also calculate the apparent SNR and CNR in the reconstructed images and statistically evaluate the general image quality with blind review from two cardiologists. In addition, the utilization of the refocusing mechanism in a spiral-in/out bSSFP sequence to separate fat and water is demonstrated.

As mentioned above, a spiral trajectory is more time-efficient and therefore can be combined with different types of sequences, including bSSFP, gradient echo (GRE) and turbo spin echo (TSE) sequences in different dynamic MRI applications. Velopharyngeal insufficiency (VPI) is a malfunction of a velopharyngeal mechanism resulting in a hypernasal voice resonance and nasal emissions while talking. It is commonly caused by a cleft palate and requires a repair surgery. Real-time velum imaging during speech can be used for evaluating velopharyngeal closure to provide the opportunity to improve diagnosis and surgical planning in patients with VPI. Spiral RF and/or gradient spoiled real-time GRE sequences can be used here to reduce the scan time. However, as the requirements for temporal and spatial resolution and SNR are very demanding in this application, spatial parallel imaging techniques using multiple receiver coils and temporal parallel imaging techniques exploiting the temporal redundancy in an image series are also applied in combination with the spiral trajectory for a further reduction of the scan time. In addition, in this particular application, $B0$ field inhomogeneity is very severe due to the air-tissue boundary and hence requires correction. Therefore, **Specific Aim #2 is to implement the spiral GRE sequence on the scanner for real-time velum imaging and reconstruct the images using spatial and temporal parallel imaging techniques with off-resonance correction.** VPI diagnostic study and velum muscle modeling based on the dynamic image series can be performed afterwards in collaborations with other researchers.

Although the spiral trajectory is an important alternative in many dynamic MRI applications, the Cartesian trajectory is still dominant clinically. However, the relatively long scan time with the Cartesian trajectory has always been a challenge for researchers and thus many techniques have been developed to reduce scan time without degrading the image quality. The effects of spatial parallel imaging techniques such as SENSE [18] and GRAPPA [19] have been widely demonstrated in various applications. In addition, various temporal parallel imaging techniques have also been developed to exploit the temporal redundancy in the dynamic image series and some of them have been combined with spatial parallel imaging techniques. However, these temporal parallel imaging techniques may suffer from temporal blurring, sensitivity to chest movements, inability to do real-time reconstruction or long reconstruction time and few have been compared and evaluated in clinical applications. The Kalman filter is a robust linear filter which is capable of real-time tracking and has been successfully adopted in real-time cardiac MRI with a non-Cartesian trajectory and also combined with SENSE [20, 21]. However, the direct application to a Cartesian trajectory is limited by model assumptions and the combination with GRAPPA has not been realized. Therefore, **Specific Aim #3 is to implement a new Cartesian Kalman filter model in real-time cardiac function MRI including combinations with both SENSE and GRAPPA and evaluate the performance of the model by comparing it with other techniques.** Simulation studies using a numerical phantom and retrospectively undersampled in-vivo data are performed as well as experiments on healthy volunteers. The evaluation is realized by blind review from two cardiologists.

1.2 Dissertation Overview

The remainder of this dissertation is organized as follows:

Chapter 2 talks about several technical issues in spiral image reconstruction including off-resonance correction, trajectory infidelity correction and DCF calculation as the basis for the dynamic spiral applications to be discussed later. Instead of providing a comprehensive overview of this giant topic, we focus on several methods currently used in the lab. The limitations of these methods are also discussed.

Chapter 3 focuses on the comparison of radial, spiral-out and spiral-in/out bSSFP sequences in real-time cardiac function MRI. First the gradient design for the two spiral sequences is introduced with the gradient moment analysis. Then the experiment setup is introduced followed by the theoretical and experimental image comparison methods. Finally the comparison results and fat-water separation are reported.

Chapter 4 focuses on the spiral parallel imaging techniques and the application in real-time velum imaging. First the spiral spatial and temporal parallel imaging techniques are introduced followed by the off-resonance correction. Then the spiral sequence implementation and the experimental setup are introduced. Finally the primary experimental results are reported.

Chapter 5 studies the Cartesian Kalman filter techniques focusing on real-time cardiac function MRI. The basic Kalman filter model and the combination with SENSE and GRAPPA are introduced followed by simulation and experimental methods. The results of the simulation and experiment are then reported. Finally, the possible extension of this model is discussed.

Chapter 6 gives the conclusions for all three research aims and summarizes the contributions of the author and the collaborators.

Chapter 2

Spiral Image Reconstruction and Corrections

2.1 Introduction

Instead of simply performing a fast Fourier Transform (FFT) with a Cartesian k-space trajectory, image reconstruction with a spiral trajectory is far more complicated due to the offsets of the sampled k-space points from the Cartesian grids and the non-uniform sampling density. Conjugate phase (CP) reconstruction [22] is a common approach for non-Cartesian image reconstruction, described by

$$m(\mathbf{r}) = \int_t W(t)s(t)e^{i2\pi\mathbf{k}(t)\cdot\mathbf{r}}dt \tag{2.1}$$

in which $W(t)$ is the DCF. The direct calculation of $m(\mathbf{r})$ in the above equation is very time consuming and thus the gridding method is generally used for simplification with the following basic steps: 1) compensate the non-uniform sampling density by multiplying each acquired data with the corresponding DCF; 2) gridding: convolve the acquired data with a Kaiser-Bessel kernel to get the value at each Cartesian grid (oversampling is usually performed at this step); 3) 2D FFT; 4) cut the edge of the image (depending on oversampling ratio) and deapodize to eliminate the effect of the Kaiser-Bessel kernel.

However, the above reconstruction method is based on an ideal imaging system in which the phase dispersion at each pixel is only from the gradient fields and the k-space trajectory is exactly what we designed. In reality, off-resonance effects and trajectory infidelity are inevitable and can bring in severe image artifacts so that corrections during image reconstruction are required. In addition, even though the DCF is well studied for a traditional constant density spiral trajectory, for a variable density spiral trajectory in which undersampling is allowed in the outer k-space [23,24], the calculation of the DCF needs to be re-examined. The following sections will focus on these technical issues.

2.2 Off-Resonance Correction

Off-resonance effects can come from B_0 field inhomogeneity due to main field inhomogeneity and susceptibility-variation-induced field inhomogeneity, concomitant gradient fields and chemical shift. If the local off-resonance information is available, it can be incorporated into equation (2.1) as

$$m(\mathbf{r}) = \int_t W(t)s(t)e^{i2\pi\mathbf{k}(t)\cdot\mathbf{r}}e^{i(\Delta\omega(\mathbf{r})t+\phi_c(\Delta\omega_c(\mathbf{r}),t))}dt \qquad (2.2)$$

in which $\Delta\omega(\mathbf{r})$ is the local off-resonance frequency due to B_0 field inhomogeneity and therefore also called a field map and $\phi_c(\Delta\omega_c(\mathbf{r}), t)$ is the phase due to the concomitant gradient field. The influence of chemical shift is omitted here for simplicity, since it is often related to the fat content in the image and therefore depends on the specific application.

Various methods have been developed to acquire the local field map $\Delta\omega(\mathbf{r})$ and can be categorized into two groups depending on whether or not additional scans are required. For the first category, a low resolution field map is usually acquired with two single shot spirals having different echo times to approximate the actual field map due to the limitation of scan time [25]. For the second category, the images are reconstructed with all possible off-resonance frequencies and the actual local off-resonance frequency is determined via minimization of a pre-defined cost function, which is generally chosen as the imaginary part of the image, as the on-resonance image phase is assumed to be zero [26]. However, this method suffers from spurious minima due to the 2π cycle of the phases and is computationally expensive, as the range of possible off-resonance frequencies is very large. A recently developed semi-automatic method combines these two categories by acquiring a low resolution field map and using this map to delimit the search range of local off-resonance frequencies for the minimization problem so that a more accurate field map can be acquired with greatly reduced spurious minima and computation time [27]. The phase term $\phi_c(\Delta\omega_c(\mathbf{r}), t)$ can be approximated from the lowest order of the concomitant gradient field given as $\phi_c(\Delta\omega_c(\mathbf{r}), t) = \Delta\omega_c(\mathbf{r})t_c$. The detailed calculation of $\Delta\omega_c(\mathbf{r})$ and t_c are given in [28] and are omitted here for simplicity.

Comparing equation (2.2) with equation (2.1), we see that the conventional gridding method can no longer be applied due to the spatially variant phase term $\Delta\omega(\mathbf{r})t + \phi_c(\Delta\omega_c(\mathbf{r}), t)$. A fast conjugate phase reconstruction method based on a Chebyshev approximation has instead been developed [29], expressed as

$$m(\mathbf{r}) = \sum_{k=0}^{N-1} \omega_k(\Delta\omega(\mathbf{r}), \Delta\omega_c(\mathbf{r}), \tau) I_k(\mathbf{r}) - \frac{1}{2} I_0(\mathbf{r}) \tag{2.3}$$

where τ is the readout length, $I_k(\mathbf{r})$ are base images, $\omega_k(\Delta\omega(\mathbf{r}), \Delta\omega_c(\mathbf{r}), \tau)$ are constant coefficients whose values depend on the B_0 field inhomogeneity, the concomitant gradient field and the readout length. The base images $I_k(\mathbf{r})$ are calculated with

$$I_k(\mathbf{r}) = \int_t \left(\frac{2t}{\tau} - 1\right)^l W(t)s(t)e^{i2\pi\mathbf{k}(t)\cdot\mathbf{r}} dt \tag{2.4}$$

in which the gridding method can be used for rapid computation.

This off-resonance correction method has proved its effectiveness in many spiral applications and the computation time is greatly reduced compared with other conjugate phase reconstruction methods; however, for some dynamic applications in which the spiral readout time is very short so that the off-resonance effects are relatively benign, the adoption of this method is unnecessary as its computation load is still too high to realize real-time reconstruction with moderate hardware, which is preferred in such applications. Therefore, a linear approximation of the low resolution field map given as $\Delta\omega(\mathbf{r}) = 2\pi(f_0 + \alpha x + \beta y)$ is used instead and the concomitant phase term is omitted as the image plane can be moved to the center of the magnet to minimize the concomitant gradient fields. The off-resonance correction can then be performed by demodulating the data at center frequency f_0 and revising the k-space trajectory to include the α and β terms [25] before the conventional gridding is performed. This method adds little additional computation and thus is suitable for real-time reconstruction.

2.3 Trajectory Infidelity Correction

From Maxwell's equations, time-varying magnetic fields resulting from gradients in MRI pulse sequences will induce currents in conducting structures within the magnet, gradient coils and RF coils. These induced currents are called eddy currents and create unwanted magnetic fields that are detrimental to image quality. The z component of the magnetic field created by eddy currents, $B_z(\overrightarrow{x}, t)$ is the dominant component and has the largest effect on image quality. It can be expanded using Taylor expansion [30] as

$$B_z(\overrightarrow{x}, t) = B_0(t) + \overrightarrow{x} \cdot \overrightarrow{g}(t) + \cdots \tag{2.5}$$

The first term is called the B_0 eddy current and the second term is called the linear eddy current. Higher order terms are not usually considered. The effect of the B_0 eddy currents is to generate an additional time-varying magnetic field on the z axis and change the center resonance frequency. The effect of the linear eddy currents $\overrightarrow{g}(t)$ is to add time-varying gradients to the specified gradient waveforms on three physical axes and affect the k-space trajectory. It is demonstrated in [31] that B_0 eddy currents are very small and can usually be ignored, but the linear eddy currents have much more impact on the trajectory and need to be corrected during image reconstruction.

In addition to the linear eddy currents, the deviation of the actual k-space trajectory from the theoretical trajectory also comes from the anisotropic delay between the actual and the specified gradient waveforms on three physical axes. In fact, the actual trajectory given an image plane and a set of spiral parameters can be measured using the modified modified Duyn's method [32, 33] by exciting two symmetric off-center slices along the physical axis along which the trajectory is measured. However, this method is impractical during human imaging as the trajectory measurement takes a very long scan time and the measurement has to be re-performed whenever the image plane or the spiral parameters are changed. Therefore, we aim to build a model to estimate the actual trajectory considering the two sources of trajectory infidelity.

The k-space trajectory due to the linear eddy currents $K_e(t)$ can be expressed as

$$\begin{aligned} K_e(t) &= \int_0^t s(\tau) \otimes H(\tau) d\tau \\ &\approx A \int_0^t G_d(\tau) d\tau + B \int_0^t K_d(\tau) d\tau \\ &= AK_d(t) + B \int_0^t K_d(\tau) d\tau \end{aligned} \tag{2.6}$$

in which $s(\tau)$ is the slew rate, $H(\tau)$ is the impulse response function characterizing the linear eddy currents, A and B are the constants corresponding to the 0^{th} and 1^{st} order Taylor expansion of the impulse response function $H(\tau)$, and $K_d(t)$ is the calculated trajectory given a specific gradient delay on one physical axis. The detailed derivation of this equation is given in [33] and is omitted here. Therefore, we have the estimated trajectory $K(t)$ on each physical axis to be

$$K(t) = K_d(t) + K_e(t) = (1 + A)K_d(t) + B \int_0^t K_d(\tau) d\tau \tag{2.7}$$

The values of $A' = 1 + A$, B and the gradient delay on three physical axes can be determined using a least square fit with the measured trajectory during a phantom experiment and are assumed to be invariant for all image planes and spiral parameters. The estimated trajectory calculated using equation (2.7) can be used in image reconstruction, instead of a theoretical trajectory that only considers an isotropic gradient delay, which is called a single-delay trajectory.

Figure 2.1 shows the comparison of the calculated single-delay trajectory, the measured trajectory and the estimated trajectory in a spiral-in/out experiment. The mean square difference between the estimated trajectory and the measured trajectory is 0.0962 while the difference between the single-delay trajectory and the measured trajectory is 0.2152. Figure 2.2 shows the differences between the images reconstructed using the single-delay trajectory and the measured trajectory (left) and the images reconstructed using the estimated trajectory and the measured trajectory (right). The mean square value of the difference images reduces from 0.0177 to 0.0112 with the estimated trajectory.

2.4 Cut-Off Voronoi DCF

Variable density spiral scanning is a more efficient way to acquire k-space data and can reduce the amplitude of low-frequency aliasing artifacts compared with constant density spiral scanning. Therefore, it is widely used in many dynamic MRI applications. However, though the outer k-space contains little energy, high-frequency aliasing due to undersampling is sometimes still noticeable, especially when the undersampling ratio becomes very large. To reduce the high-frequency aliasing without affecting the low-frequency k-space data, we can modify the DCF

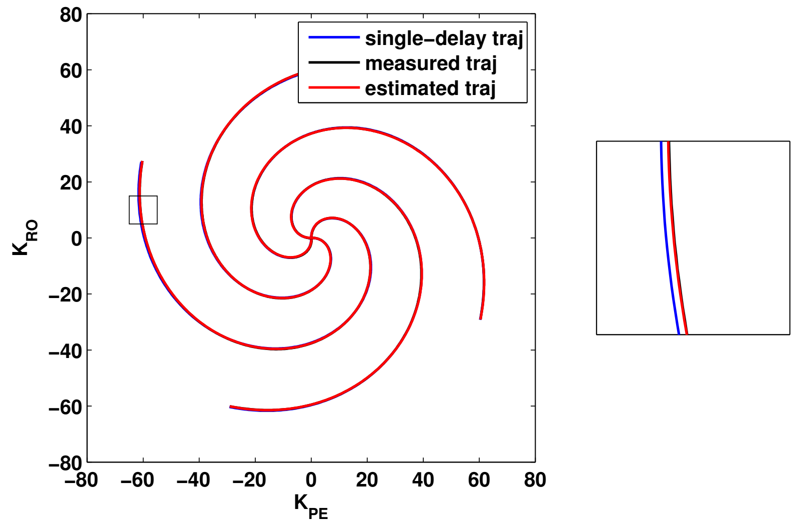

Figure 2.1: *Comparison of the single-delay trajectory, the estimated trajectory and the measured trajectory. The right figure is the enlarged area indicated by the box on the left figure.*

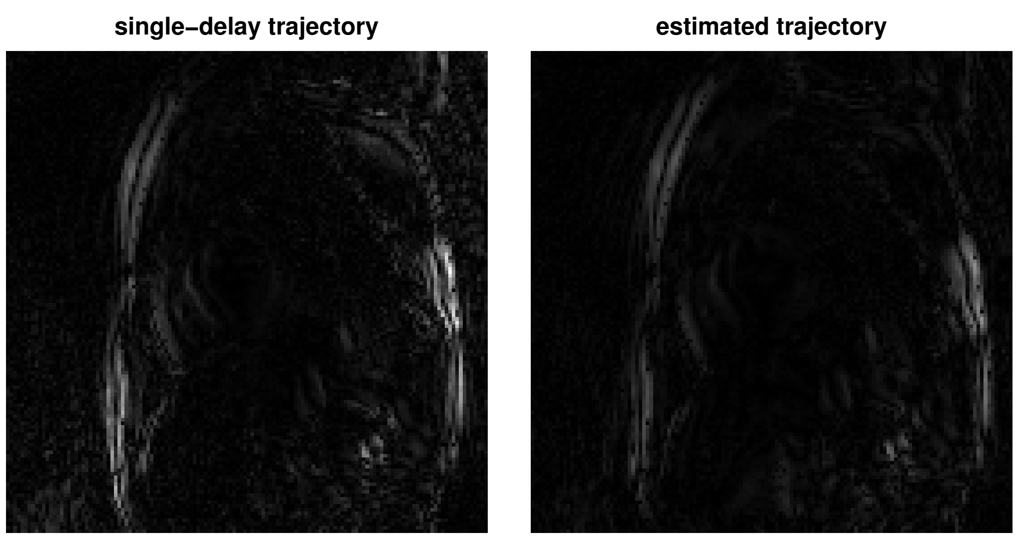

Figure 2.2: *Difference images between the single-delay trajectory and the measured trajectory (left) and the estimated trajectory and the measured trajectory (right).*

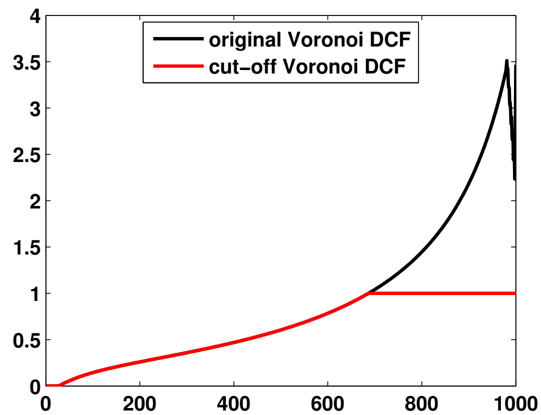

Figure 2.3: *The original Voronoi DCF (black) and the cut-off Voronoi DCF (red). The fluctuation of the original Voronoi DCF at the end is due to the selection of an encompassing circle for the entire k-space trajectory.*

to suppress the k-space data in the undersampled region [9, 10]. The DCF for a spiral trajectory is often calculated as the area of the Voronoi region at each k-space point due to its simplicity and robustness [7] and is therefore referred to as the Voronoi DCF. With a variable density spiral trajectory, the undersampled regions can be easily identified from the Voronoi DCF, as the Voronoi area of a critical sampled point is just one with the unnormalized k-space trajectory. Therefore, we can cut off the original Voronoi DCF at this undersampling threshold and use a flat DCF for the undersampled k-space data as shown in Fig. 2.3.

The theoretical point spread functions (PSF) with a variable density k-space trajectory using the original Voronoi DCF and the cut-off Voronoi DCF are calculated and plotted in figure 2.4. It is shown that the sidelobes are greatly suppressed with the cut-off Voronoi DCF and the main lobe width is only slightly increased. The reason for the main lobe width increase is because the suppression of the k-space data in the undersampled region will effectively decrease the spa-

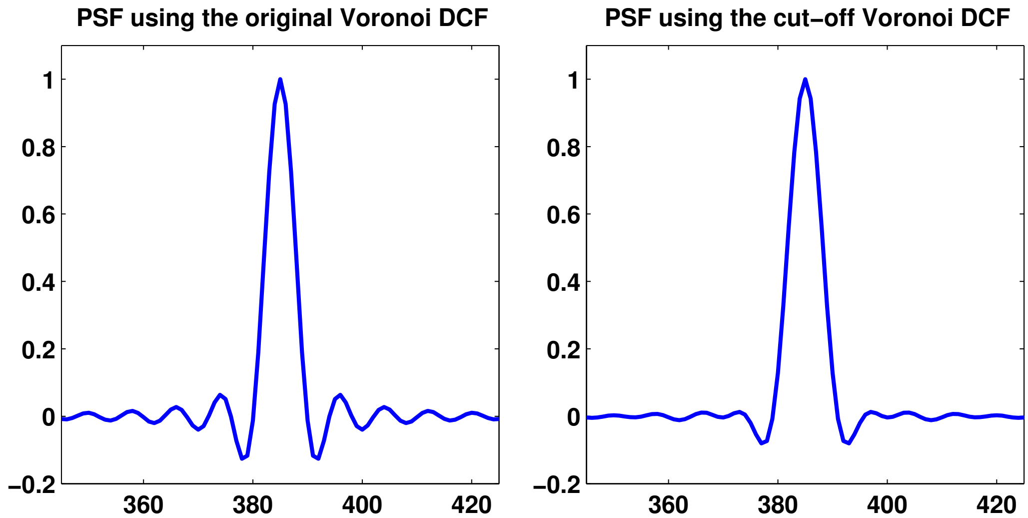

Figure 2.4: *Theoretical PSFs for the original Voronoi DCF (left) and the cut-off Voronoi DCF (right).*

tial resolution. Figure 2.5 shows the reconstructed images with these two DCFs. A decrease of overall aliasing is observed with the cut-off Voronoi DCF, and the blurring related to the increase of the main lobe width is very small. Therefore the cut-off Voronoi DCF is used for the image reconstruction with a variable density spiral trajectory.

2.5 Discussion

In this chapter we introduced spiral reconstruction methods focusing on three technical issues: off-resonance correction, trajectory infidelity correction and cut-off Voronoi DCF calculation. The purpose is to reduce the image artifacts in spiral scanning, since the spiral trajectory is much more sensitive to these effects compared with the Cartesian trajectory.

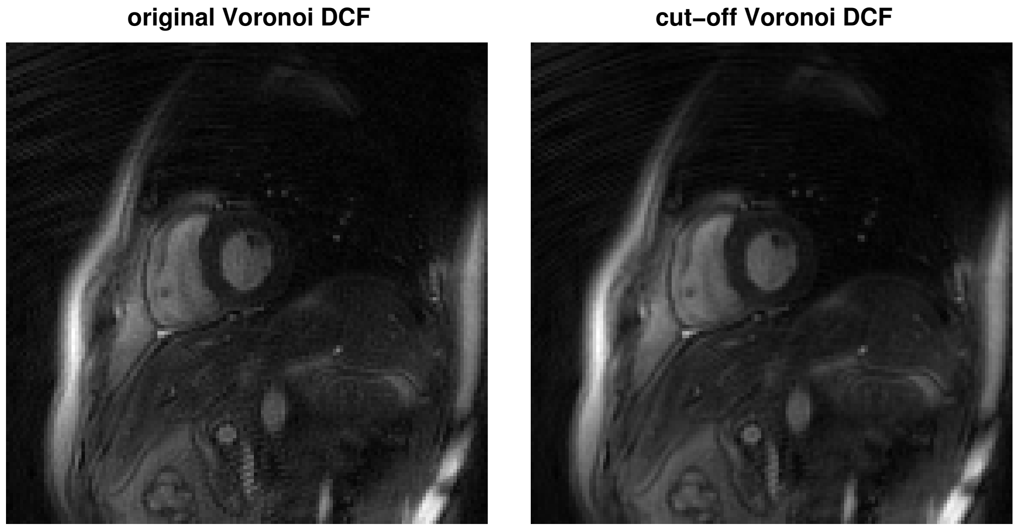

Figure 2.5: *Cardiac spiral-out bSSFP images using variable density spiral with the original Voronoi DCF (left) and the cut-off Voronoi DCF (right).*

For off-resonance correction, we introduced two commonly used methods: fast conjugate phase reconstruction based on a Chebyshev approximation and linear correction. The first method is more effective in terms of deblurring as it achieves a high resolution field map and a phase map due to the concomitant gradient fields and reconstructs each pixel at the given off-resonance frequency, but the reconstruction time is relatively long. The second method is usually applied when the off-resonance effects are not severe and the demand for reconstruction speed is high. Nevertheless, neither of these two methods takes chemical shift into consideration due to the complexity of the problem. In fact, the blurring caused by the fat component of an image can be very severe in some applications inhibiting the wide adoption of spiral scanning. One possible way to handle this is to ignore the fat and achieve a fat-suppressed field map to only de-blur the water component when the fat blurring is outside the region of interest (ROI). A detailed description of this issue is beyond the scope of this dissertation.

In the trajectory infidelity correction, there are two major limitations in the current model. First, one important assumption of this model is that the eddy currents due to the gradients in a prior repetition will not affect the trajectory of subsequent repetitions. This is generally true with a long TR; however, for some rapid sequences such as SSFP and TSE, this assumption may be invalid and the effects have to be considered. Second, the effect of automatic pre-compensation of the gradient system is not considered so that the actual eddy currents may differ from the theoretical ones. As the mechanism of pre-compensation is unknown for the Siemens scanner, the refinement of the model is very difficult. Therefore, even though in theory the constants in trajectory estimation only depend on the specific gradient system, we determined that the constants for the spiral-out trajectory and the spiral-in/out trajectory achieved from the least square fit with the measured trajectory are significantly different on the same scanner and hence each set of constants is used for a given type of trajectory in practice.

The usage of the cut-off Voronoi DCF can suppress the high-frequency aliasing for a variable density spiral trajectory with a minor sacrifice of spatial resolution. This is also an SNR optimal way in terms of data processing. However, the optimality of this method is not validated and further study is required on this topic.

Chapter 3

Comparison of Radial, Spiral-out, Spiral-in/out bSSFP Sequences in Real-Time Cardiac Function MRI

3.1 Introduction

In real-time cardiac function MRI, a series of cardiac images are continuously acquired without gating under breath-held or free-breathing conditions to avoid the effects of arrhythmia on the gating signal and data acquisition. However, the requirements for high temporal and spatial resolution and SNR are challenging. Non-Cartesian imaging techniques are advantageous in terms of reduced scan time and thus are important options in this application.

As two major representatives of non-Cartesian imaging, radial bSSFP reduces scan time through outer k-space undersampling, whereas spiral bSSFP reduces scan time primarily by scanning more of k-space with a spiral pattern in a given

TR, with undersampling possible using a variable density trajectory. Both radial and spiral bSSFP sequences are inherently robust to flow and motion artifacts because they repeatedly sample the center of k-space, and spiral scans do not accumulate gradient moments. Spiral bSSFP is more sensitive to the off-resonance effects while radial bSSFP suffers more from the streaking artifacts due to undersampling. One goal of this study is to compare radial and spiral bSSFP sequences in real-time cardiac function MRI.

In addition to the traditional spiral bSSFP sequence, which we will call the spiral-out bSSFP sequence, we also want to develop a new spiral-in/out bSSFP sequence to realize the refocusing mechanism by moving TE to the center of TR as in a typical bSSFP sequence. The advantages of the refocusing mechanism include increased SNR since all spins will align at the center of the TR and the phase cycle property, which can be used for fat-water separation. In addition, the spiral-in/out bSSFP sequence faciliates gradient moment rephaser design compared with the spiral-out bSSFP sequence because it can realize 1^{st} order gradient moment nulling via symmetry as long as the 0^{th} order gradient moment is nulled, while the spiral-out bSSFP requires a specifically designed rephaser to null both the 0^{th} and 1^{st} order gradient moments.

In the remainder of this chapter, we will first introduce the gradient design methods for the spiral-out and spiral-in/out bSSFP sequences, including gradient moment analysis. We use the Siemens cardiovascular package to implement the radial bSSFP sequence. Next we will introduce the experimental setup and the comparison schemes followed by the comparison results. Finally, fat-water separation with the spiral-in/out bSSFP sequence is discussed.

3.2 Gradient Design

In a typical bSSFP gradient design, the gradient-induced dephasing within one TR should be exactly zero; in other words, the 0^{th} order gradient moment m_0 at the end of TR is zero. Moreover, in real-time cardiac imaging, as well as many other applications in which in-plane motion and flow effects cannot be omitted, the 1^{st} order gradient moment m_1 at the end of TR should also be zero to suppress the constant flow induced dephasing [34]. Higher-order gradient moment nulling could theoretically provide further dephasing suppression; however, this usually requires additional rewinding gradients, so that the TR would be prolonged, making the sequences more susceptible to banding artifacts due to inhomogeneity and complicating the design process. In practice, a gradient design satisfying $m_0 = 0$ and $m_1 = 0$ is required and higher order gradient moments are not considered.

3.2.1 Spiral-Out Gradient Design

Spiral-out gradients are comprised of the desired spiral readout gradients and a following rephaser nullifying the 0^{th} and 1^{st} order gradient moments of the readout gradients. The algorithm introduced by Meyer et al. [2] is used for spiral readout gradient design. The desired k-space trajectory is

$$k(\tau) = A\tau \exp^{i\omega\tau}, \tag{3.1}$$

where τ is a function of time and ω is a parameter essentially determined from the Nyquist sampling criterion. In an N-interleaf constant density spiral trajectory design, the spacing of spiral arms of one interleaf on one axis should match the Nyquist sampling frequency, shown as

$$2\pi A/\omega = 1/FOV/N, \tag{3.2}$$

in which FOV is the field of view along the corresponding axis. In variable density spiral trajectory design [23, 24], this spacing is a function of the radius of the trajectory. There are many ways to design such a function by varying ω, and the comparison and evaluation of these different methods is still an open question. Here we simply adopt a linear variable density design, in which ω is linearly decreased with each gradient sample from ω_{max} at the center to ω_{min} at the edge of the k-space.

For the rephaser design satisfying the 0^{th} and 1^{st} order gradient moments nulling requirements, we use the algorithm introduced by Nayak et al. [16] to simultaneously compensate the 0^{th} and 1^{st} gradient moments via several sets of triangle gradients. In this algorithm, first the spiral readout gradients are rotated so that the gradients on one axis end with zero amplitude, then two to three sets of triangle gradients are used with lengths solved from the gradient moment nulling equations, and finally the gradients are rotated back. Figure 3.1 shows the resulting gradients and the corresponding trajectory of a single interleaf in a 32-interleaf variable density design.

Now we have generated the gradients for one interleaf in an N-interleaf design; in order to get the entire gradients, we can just rotate these gradients by $2\pi/N$ each time. In addition, reordering the interleaves in a bit-reversed way to increase the distance of k-space samples between consecutive interleaves has been shown

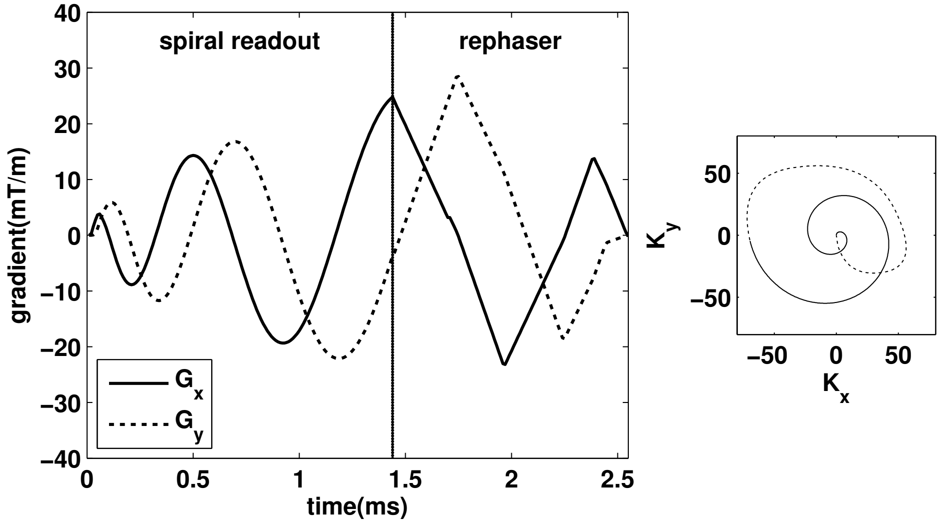

Figure 3.1: *Spiral-out bSSFP gradients (left) and the corresponding k-space trajectory(right) of one interleaf in a* 32*-interleaf variable density design. The density decreases from* 1.2 *in the center to* 0.4 *in the edge of the k-space. A density of* 1.0 *corresponds to the Nyquist rate.*

to be beneficial for dynamic imaging [35]. Complete bit-reversed order only exists for a number in form of 2^m in which m is an integer, so that for arbitrary interleaf number N, the complete bit-reversed order cannot be realized. Here we develop a simple algorithm to get the order for an arbitrary N by using the bit-reversed order table of the smallest 2^m number larger than N and throwing out the order number that is equal or larger than N. For example, if $N = 6$, first we have a bit-reversed order table for 8 to be $[0, 4, 2, 6, 1, 5, 3, 7]$ and then we throw out 6 and 7 in the table to get the order table for $N = 6$ as $[0, 4, 2, 1, 5, 3]$. The entire gradients are then generated after rotation and reordering.

3.2.2 Spiral-In/Out Gradient Design

To generate the desired spiral-in/out trajectory, four steps are required: 1) generate the desired spiral-out arm of the spiral-in/out readout gradients; 2) generate time-optimal transition gradients following the spiral-out arm to move the k-space trajectory to the origin and simultaneously reduce the gradient magnitude to zero; 3) time reverse the previous gradients and put the reversed gradients in front, so that the k-space trajectory is at the origin at the midpoint of the entire gradient waveform; 4) rotate and reorder to get all of the gradient waveforms.

The spiral-out arm is generated using the same algorithm as in the spiral-out bSSFP readout gradient design introduced in the previous subsection; variable density spiral design is preferred as well. However, the calculation of ω is different, since each interleaf of spiral-in/out readout gradients can be viewed as two spiral-out arms symmetric over the origin if the traversal direction of the trajectory is not considered; therefore, if the interleaf number is N, we have

$$2\pi A/\omega = 1/FOV/2N. \tag{3.3}$$

After the spiral-out arm of spiral-in/out gradients is designed, transition gradients that can move the k-space trajectory back to the origin and reduce the gradient magnitude to zero are required. Instead of using the straightforward method of first using winding down gradients to reduce the gradient to zero and then adding a set of triangle gradients to compensate the 0^{th} order gradient moment, we develop an algorithm to simultaneously achieve both goals to shorten the rephaser length. First we calculate the 0^{th} moment of the winding down gradients and compare this with the negative of the 0^{th} moment of the spiral-out arm gradients. If the former is smaller, which means we are under-compensating the spiral-out arm with such winding down gradients, a set of triangle gradients are inserted between the spiral-out arm and the winding down gradients to most efficiently compensate the 0^{th} moment; if the former is larger, which means we are over-compensating the spiral-out arm, a set of triangle gradients are added after the winding down gradients. As shown in Fig. 3.2, the transition gradients of the rephaser start with the last spiral-out readout gradients for both Gx and Gy. For Gx, the winding down gradients over-compensate the spiral-out arm so that a set of triangle gradients are added after the gradients are reduced to zero. For Gy, the winding down gradients under-compensate the spiral-out arm so that we first increase the gradient amplitude and then add the winding down gradients to more rapidly move the k-space location to the center. The peak amplitude of the transition gradients is calculated with the 0^{th} gradient moment nulling requirements.

The maximum possible slew rate is used on each axis; however, considering the fact that double-oblique slices are usually used in cardiac imaging, it should be guaranteed that the maximum combined slew rate $S = \sqrt{S_{RO}^2 + S_{PE}^2 + S_{SS}^2}$, in which S_{RO}, S_{PE} and S_{SS} respectively mean the slew rate on readout direction, phase encoding direction and slice selection direction, is smaller than the specified slew rate limit S_{max}. The optimal or near-optimal distribution of S_{RO}, S_{PE} and S_{SS} can be achieved through an iterative search until a balance is struck between optimality and computation time.

By just time reversing the previous gradients, we not only null the 0^{th} gradient moment, but also null the 1^{st} gradient moment. $m_0 = 0$ at the end of TR is easy to prove since the transition gradients already compensate the spiral-out arm of the spiral-in/out readout gradients, and time reversing the gradients does not change the 0^{th} gradient moment. The 1^{st} gradient moment m_1 at the end of TR can be calculated as:

$$\begin{aligned} m_1 &= \int_0^t G(u)udu = \int_0^{t/2} G(u)udu + \int_{t/2}^t G(u)udu \\ &= \int_0^{t/2} G(u)udu + \int_0^{t/2} G(t-u)(t-u)du \\ &= \int_0^{t/2} [G(u) - G(t-u)]udu + t\int_0^{t/2} G(t-u)du \end{aligned} \tag{3.4}$$

in which $G(t)$ is the gradient waveform. From the previous design steps, we can get $G(u) = G(t-u)$ due to symmetry and $\int_0^{t/2} G(t-u)du = 0$; consequently, $m_1 = 0$. Figure 3.2 shows the resulting gradients and the corresponding trajectory of a single interleaf in a 32-interleaf variable density design.

The rotation and reordering step is similar with spiral-out gradient design, except the rotation angle is π/N for each interleaf since one interleaf would overlap with itself after a π rotation.

The symmetric property of the gradients can not only facilitate the rephaser design as just mentioned but also shorten the minimum TR compared with the spiral-out bSSFP sequence, because the prephaser and the rephaser gradients here can overlap with the slice-selection rephaser and prephaser gradients. In the spiral-out bSSFP sequence the overlap can only happen on one side. This shortening can also be traded for a longer spiral readout, as we will do in our experiments.

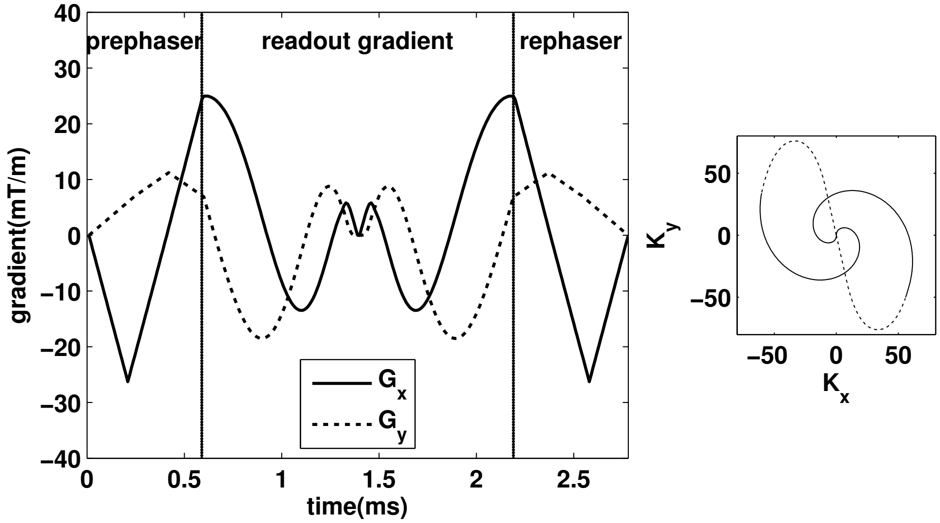

Figure 3.2: *Spiral-in/out bSSFP gradients (left) and the corresponding k-space trajectory of first two interleaves (right) in a 32-interleaf variable density design.*

3.2.3 Discussions

In both spiral-out and spiral-in/out bSSFP sequences, we realized the 0^{th} and 1^{st} order gradient moment nulling at the end of TR and did not consider the higher order moments. The resulting 2^{nd} order gradient moments for both sequences as well as the gradient moments during TR are shown in figure 3.3. We see that the spiral-out trajectory has smaller gradient moments during the readout in general than the spiral-in/out trajectory, and the 2^{nd} order gradient moment at the end of TR is very close to zero with the spiral-out trajectory while it is very large with the spiral-in/out trajectory. The reason is because even though the spiral-in/out trajectory inherits the advantage of a general spiral trajectory in terms of not accumulating gradient moments in both spiral-in and spiral-out arms, the symmetric property can amplify the remaining lower order gradient moments in both arms and lead to large high order moments. Therefore, the spiral-out bSSFP

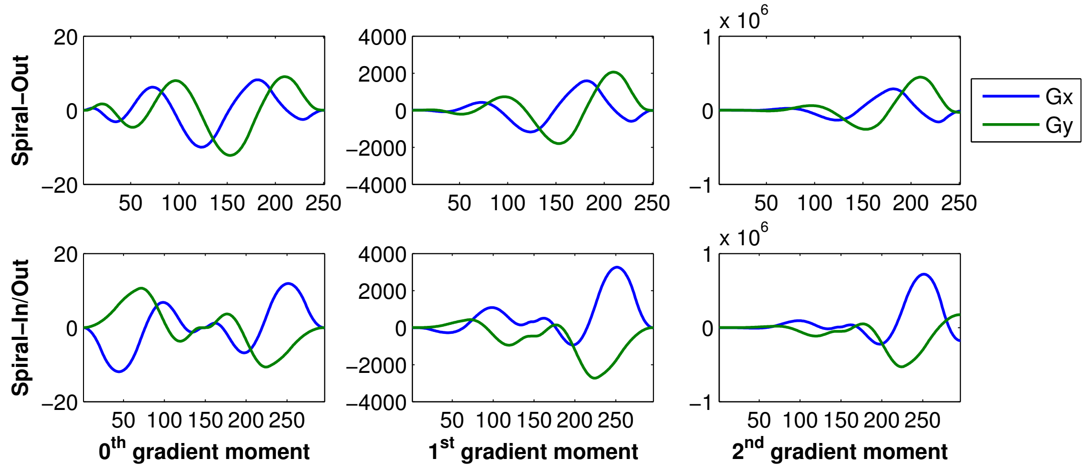

Figure 3.3: 0^{th}, 1^{st} *and* 2^{nd} *order gradient moments during one TR for both spiral-out and spiral-in/out bSSFP sequences.*

sequence will be more robust to in-plane motion and flow artifacts in theory.

In the above gradient design method for the spiral-out bSSFP sequence, there is a potential problem in the rephaser design, since the gradient amplitude limit is not considered in the calculation of the lengths of the triangle gradients. If the gradient limit is exceeded, this rephaser design will fail, because if we simply replace the triangle gradients with a set of trapezoid gradients without changing the total area, the 0^{th} order gradient moment can still be compensated but the 1^{st} order gradient moment will change. Luckily, in our current application of this sequence, the typical imaging parameters will not result in exceeding the gradient amplitude limit. However, with a smaller FOV the gradient amplitude limit is often reached and alternative design methods are required. For example, instead of using all triangles, the combination of trapezoids and triangles can be used with more parameters to be solved with the corresponding gradient moment nulling requirements.

In addition, in our current spiral-in/out design, the spiral-out arm starts at zero. In fact, the starting gradient can have arbitrary magnitude as long as the gradient amplitude limit is not exceeded. Furthermore, starting with a non-zero gradient can increase the k-space trasversal speed to reduce the time for the entire k-space coverage. However, this will lead to inaccurate k-space measurement at TE due to the gradient delays and DC artifacts. Therefore, we still choose the starting gradient to be zero to prolong the actual echo time to sweep a range around TR/2 so that a more accurate measurement at TE can be achieved with more averages.

3.3 Methods

3.3.1 Experiments

Comparison studies were performed on a Siemens Avanto 1.5 T scanner equipped with multiple surface coils. Six healthy volunteers (4 males and 2 females, ranging in age from 20 to 30) with informed consent participated in this study. For each subject, a mid ventricular short-axis view and a horizontal long-axis view were scouted in both breath-hold and free-breathing conditions. For each set of experiments, the radial, spiral-out and spiral-in/out bSSFP sequences were run consecutively with the same image slice using 8 mm slice thickness and $340 * 340$ mm^2 FOV. Other sequence parameters and the resulting spatial and temporal resolutions are given in Table 3.1. The spatial resolution here is calculated from the full width at half maximum (FWHM) of the theoretical PSFs due to the

Table 3.1: *Sequence parameters and the resulting spatial and temporal resolutions for the radial, spiral-out and spiral-in/out bSSFP sequences.*

	TR/TE (ms)	Flip Angle	# interleaf	Spatial Res. (mm^2)	Temporal Res. (Hz)
Radial	2.36/1.18	46°	48	$3.24 * 3.24$	8.83
Spiral-out	3.76/0.99	50°	32	$3.20 * 3.20$	8.31
Spiral-in/out	3.69/1.84	50°	32	$3.15 * 3.15$	8.47

non-Cartesian sampling pattern. The temporal resolution is the number of fully sampled images per second. For a fair comparison, we matched the spatial and temporal resolutions of the two spiral sequences with the radial sequence of a typical clinical scan.

In each experiment, the Siemens gradient-echo cardiac shimming [36] was used to reduce inhomogeneity. The same shim setting was used for all three sequences. For the two spiral sequences, a fat-suppressed low resolution field map was acquired using spectral-spatial RF excitation pulses [37, 38] before the real-time data acquisition. We simply assumed that the field map will not change significantly during the scan and the linear off-resonance correction method is sufficient to deblur the entire image series. The concomitant gradient field influence was greatly reduced by putting the image plane into the center of the magnet. The estimated trajectory and the cut-off Voronoi DCF calculated with the methods introduced in chapter 2 were used in the reconstruction.

Online reconstruction was implemented for all three sequences on the scanner. $2x$ view sharing was used for all three sequences to double the apparent temporal resolution. The images from each coil were separately reconstructed and combined via a sum-of-square method.

3.3.2 Comparison Methods

With the given trajectories of the radial, spiral-out and spiral-in/out bSSFP sequences, we calculated the theoretical point spread functions and the aliased energy contained in the side lobes of the PSFs.

In addition, the apparent SNR of the blood and the CNR between the blood and myocardium of a given image can be measured with a given magnitude image by dividing the mean image intensity at the blood region and the mean image intensity difference between blood and myocardium by the mean image intensity outside the chest and multiplying the results with a constant to account for the fact that the mean magnitude of the apparent noise is measured instead of its standard deviation. As the aliasing may affect the validity of the noise level measurement, it is very difficult to get the pure noise level without an additional measurement. However, this apparent SNR and CNR including the aliasing effect can better reflect the visualized image quality and are therefore compared. Other factors affecting the SNR and CNR including measurement time and theoretical signal level were also calculated and analyzed. For each dynamic image series, 5 images covering the heart cycle are selected from the dynamic data set for simplicity of the SNR and CNR measurement. The values were then averaged as the SNR and CNR for this image series. The one way analysis of variance (ANOVA) was performed to compare the different methods.

The overall image quality was also evaluated by blind rating from two experienced cardiologists on a $0-5$ scale with 5 indicating the best image quality. The results were analyzed using the paired Wilcoxon signed-rank test.

3.3.3 Fat-Water Separation

In a general bSSFP sequence, the refocusing mechanism at TE = TR/2 will result in a phase cycling property with different local off-resonance frequencies. Figure 3.4 shows the simulated bSSFP signal phase at the center of TR of the blood and myocardium pixels at 1.5 T. The phases of both pixels alternate between 0 and 180 with a period given by 1/TR. In this simulation, TR = 3.69 ms in the spiral-in/out bSSFP sequence and the corresponding period is 271 Hz. Since the resonant frequencies of fat and water at 1.5 T differ by about 220 Hz at 1.5 T due to chemical shift, the fat and water signal will have opposite phases at a large range of local off-resonance frequences. Furthermore, if the local off-resonance frequency is small, the phase of the water signal will be 0 while the phase of the fat signal will be 180. Therefore, a phase detection method [39] can be used to separate the fat pixels from the water pixels without any further measurement.

In practice, since the phase can be influenced by the surface coil among other factors, a phase correction method is required before detection. We first manually select a pixel of water/fat from the coil image and set its phase to be 0/180 and then use a region-growing method with the selected origin by breaking up the image into small cells and calculating the average phase of each cell to remove the slow-varying phase term. This technique leaves a 180-degree ambiguity in the detected phase and the phase detection can be then performed for fat-water separation.

This technique can only be applied with the spiral-in/out bSSFP sequence since the radial sequence has very small TR so that the water and fat pixels are very likely to be in the same phase band and the spiral-out sequence does not

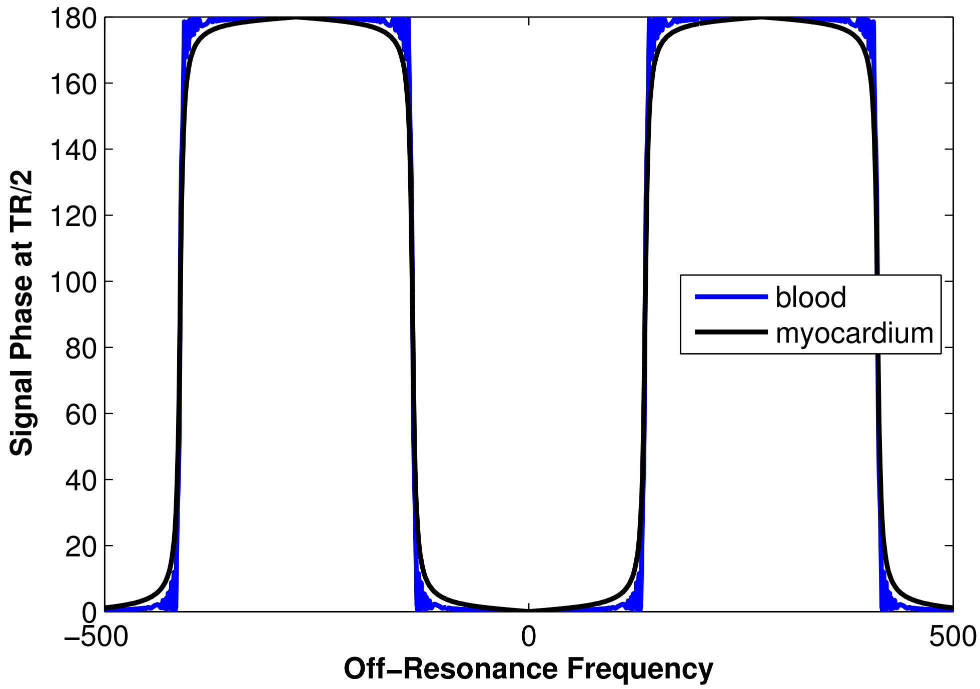

Figure 3.4: *Simulated bSSFP signal phase at the center of TR of the blood and myocardium pixel at* 1.5 *T.*

have the refocusing mechanism at the center of k-space.

3.4 Results

Figure 3.5 and Fig. 3.6 show five consecutive images from short-axis and long-axis free-breathing experiments with the radial (top row), spiral-out (medium row) and spiral-in/out (bottom row) bSSFP sequences. In the radial bSSFP images, the signal in some parts of the chest and/or back is missing; however, in spiral-out and spiral-in/out bSSFP images, the signal is intact for the chest wall and the back. The artifact level in both the spiral-out and spiral-in/out bSSFP images is much lower than that in the radial bSSFP images.

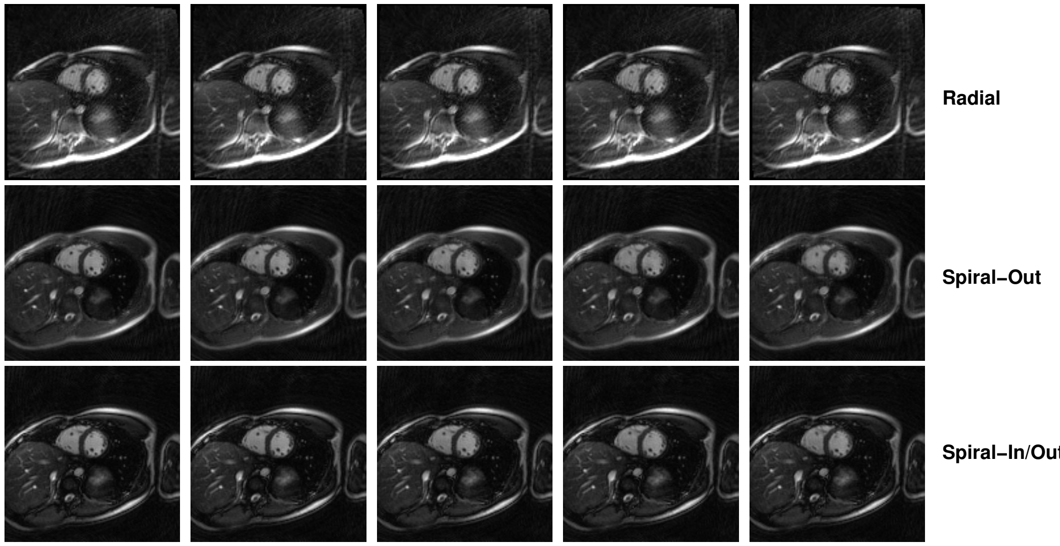

Figure 3.5: *Short-axis free-breathing images with the radial (top row), spiral-out (medium row) and spiral-in/out (bottom row) bSSFP sequences.*

3.4.1 Comparison

Figure 3.7 shows the center line of the 2D PSFs for all three sequences. The main lobes are almost coincident, indicating the same spatial resolution. However, the side lobes of the two spiral sequences have much lower values than the radial sequence, meaning the aliasing is greatly reduced. The calculated aliased energy is reduced by 85% and 82% with the spiral-out and spiral-in/out sequences compared with the radial sequence.

Figure 3.8 shows the mean apparent SNR of the blood and CNR between blood and myocardium for the radial, spiral-out and spiral-in/out bSSFP sequences with short-axis and long-axis views. The results from the breath-held and free-breathing situations are combined. Asterisks indicate a statistically sig-

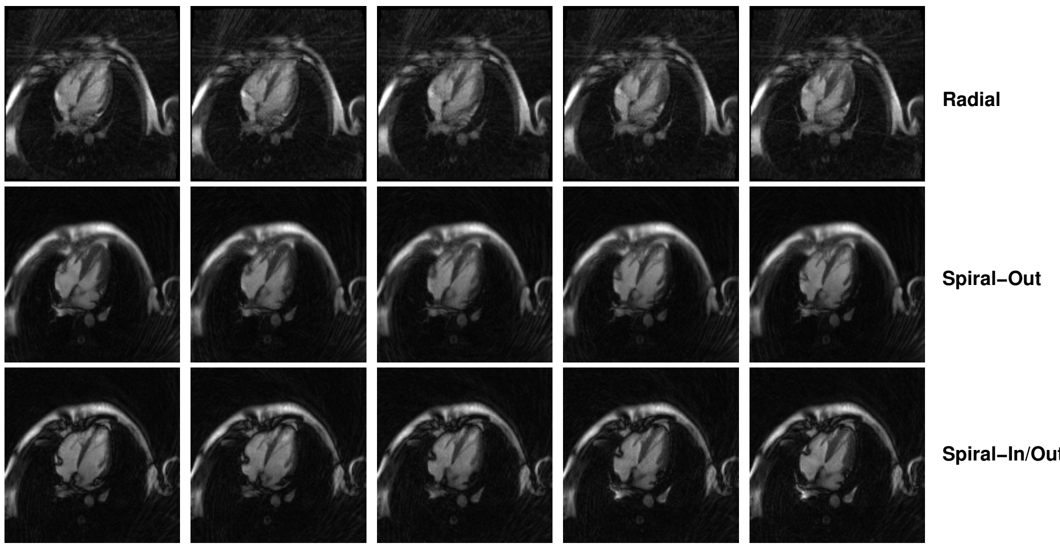

Figure 3.6: *Long-axis free-breathing images with the radial (top row), spiral-out (medium row) and spiral-in/out (bottom row) bSSFP sequences.*

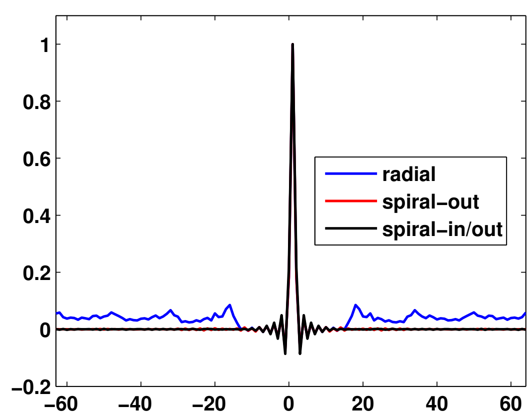

Figure 3.7: *Theoretical PSFs at the center line for radial, spiral-out and spiral-in/out bSSFP sequences with matched spatial and temporal resolutions.*

nificant difference using the ANOVA method ($p < 0.05$). The SNR and CNR are significantly higher with the spiral-in/out sequence than with the radial sequence in both short-axis and long-axis views. The spiral-out bSSFP also has higher SNR and CNR than the radial bSSFP but this difference is only statistically significant in the long-axis view.

Figure 3.9 shows the blind image rating result. We combined the results from the breath-held and free-breathing scans for each view. The image ratings are: a) short-axis view: 1) radial: 3.23±0.49, 2) spiral-out: 3.60±0.66, 3) spiral-in/out: 4.13±0.45; b) long-axis view: 1) radial: 3.19±0.55, 2) spiral-out: 3.69±0.78, 3) spiral-in/out: 4.23±0.42. The p-values of paired Wilcoxon signed-rank test under the null hypothesis that two compared sequences behave the same are a) short-axis view: 1) radial vs. spiral-out: 0.0003, 2) radial vs. spiral-in/out: 0.00003, 3) spiral-out vs. spiral-in/out: 0.101, b) long-axis view: 1) radial vs. spiral-out: 0.0024, 2) radial vs. spiral-in/out: 0.00001, 3) spiral-out vs. spiral-in/out: 0.0013. A smaller p-value indicates a more statistically significant difference. We can conclude that both spiral bSSFP sequences are favored compared with the radial bSSFP sequence for both views and the spiral-in/out bSSFP sequence performs better than the spiral-out bSSFP sequence for the long-axis view.

3.4.2 Fat-Water Separation

Figure 3.10 shows the separated water and fat images in a short-axis breath-held experiment using the spiral-in/out bSSFP sequence. The pixels of the chest wall and the fat around the myocardium are separated from the blood and myocardium

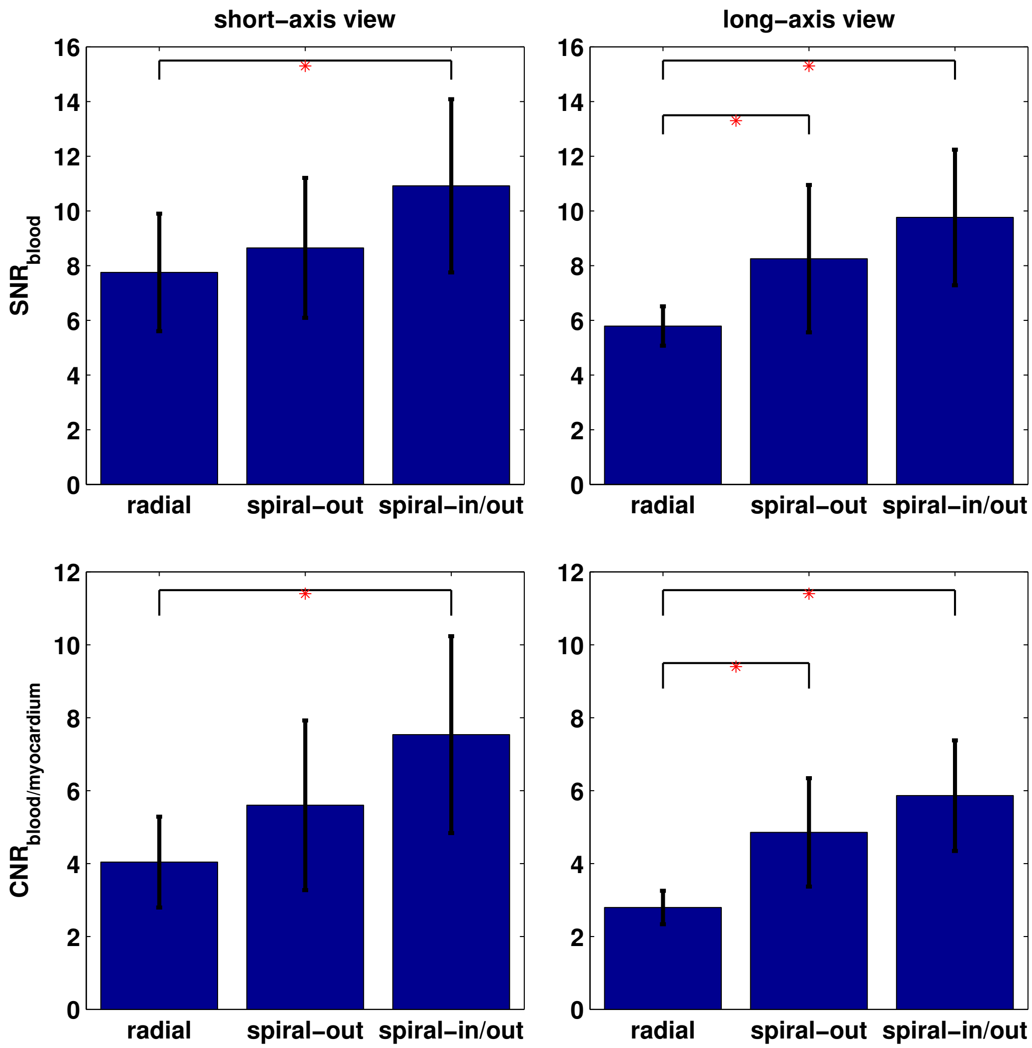

Figure 3.8: *SNR_{blood} and $CNR_{blood/myocardium}$ of the radial, spiral-out and spiral-in/out bSSFP sequences and the results of the statistical analysis. Asterisks indicate a statistically significant difference ($p < 0.05$).*

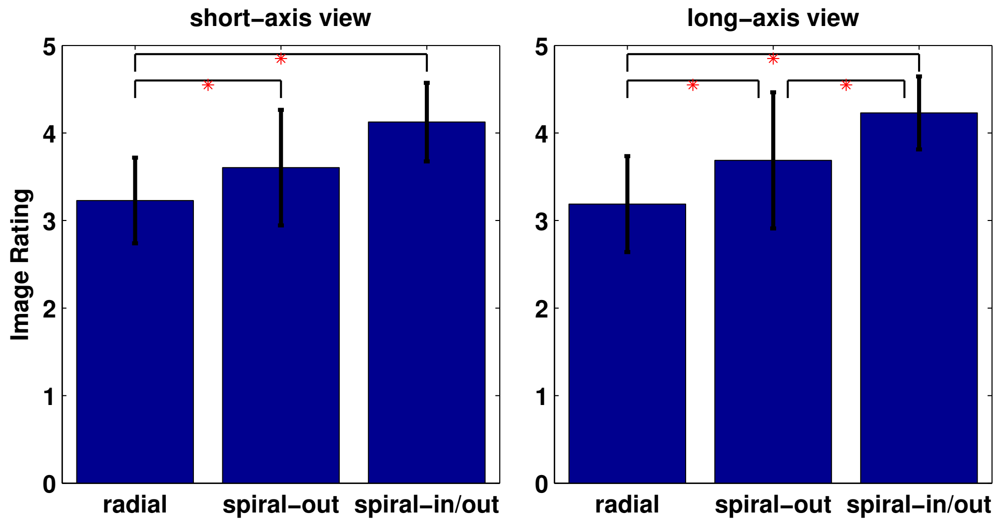

Figure 3.9: *Blind rating results of the radial, spiral-out and spiral-in/out bSSFP sequences.*

pixels. This demonstrates the effectiveness of this method and a potential advantage of the spiral-in/out bSSFP sequence with the refocusing mechanism.

3.5 Discussion

In this chapter we implemented the spiral-out bSSFP sequence and developed a new spiral-in/out bSSFP sequence to realize the bSSFP refocusing mechanism. The two spiral bSSFP sequences are experimented on the scanner and the performance in real-time cardiac function MRI are compared with the clinically adopted radial bSSFP sequence using the protocols with similar spatial and temporal resolution.

The theoretical PSFs of these three sequences were calculated and compared. The two spiral bSSFP sequences have much lower aliasing level as the magnitude

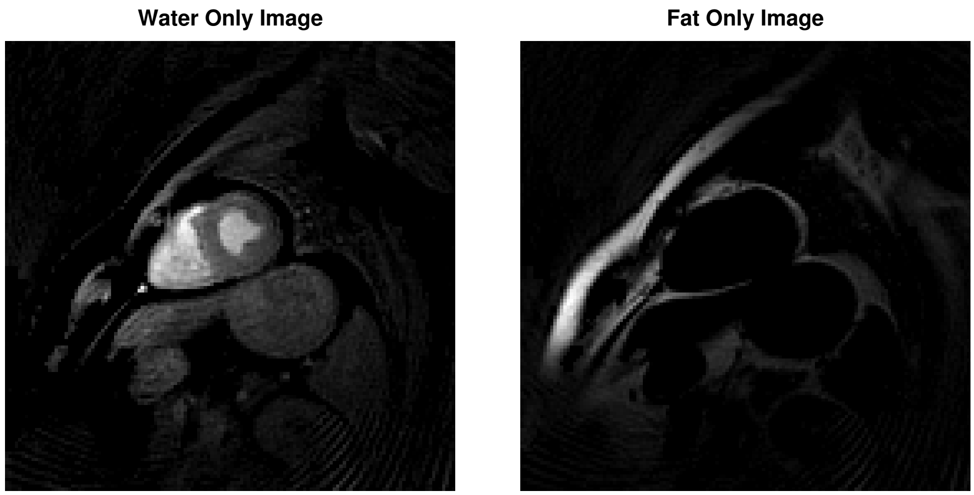

Figure 3.10: *Separated water and fat images in a short-axis breath-held experiment using the spiral-in/out bSSFP sequence.*

of the side lobes is greatly reduced. The reason is because the radial trajectory reduces the scan time by outer k-space undersampling while the spiral trajectory relies on more efficient k-space coverage per excitation. The outer k-space undersampling percentage is about 50% for the radial trajectory while it is only 20% for the variable-density spiral trajectory. The apparent SNR and CNR of both spiral bSSFP sequences are also significantly increased compared with the radial bSSFP sequence. This increase is mainly due to the reduction of aliasing level as the aliasing increases the apparent noise. The total data acquisition time with both spiral sequences is 12% longer than the radial sequence which also accounts for a slight increase of the SNR and CNR. The overall image quality of both spiral bSSFP sequences reflected by the blind rating results also show that the spiral bSSFP sequences perform significantly better than the radial bSSFP sequence.

Comparing the two spiral bSSFP sequences, the symmetry property of the spiral-in/out trajectory facilitates the gradient rephaser design and also shortens the minimum TR. The mean value of the apparent SNR and CNR increases with the spiral-in/out bSSFP sequence but the difference lacks statistical significance. The total data acquisition time and the aliasing level are very close for both sequences but the refocusing mechanism may account for the increase of the SNR and CNR, since the signal intensity at TE becomes stronger with the refocused spins. More experiments are required for the validation of this result. The overall image quality of the spiral-in/out bSSFP sequence is significantly improved compared with the spiral-out bSSFP sequence in long-axis view and also has a trend of significant improvement in short-axis view.

The refocusing mechanism achieved by the spiral-in/out bSSFP sequence can be used for fat-water separation without any additional measurements due to the phase cycling property. The result shows a very distinct separation between fat and water pixels. However, in the regions with flow and/or severe B_0 inhomogeneity the phases of fat and water are sometimes swapped during the entire image series. Further study is required for a more robust separation but this is beyond the scope of this dissertation.

There are several limitations of this study. Spatial parallel imaging techniques for both spiral and radial sequences are not applied and compared for a higher spatial and/or temporal resolution. The radial sequence we used in this study is not a state-of-the-art radial sequence, because the product package has not been updated to include the most recent developments of radial sequence design. The blind rating was also not purely blind for the radial sequence since its streaking artifacts are very conspicuous and were easily recognized by one of the cardiologists.

In conclusion, we developed a new spiral-in/out bSSFP sequence and demonstrated the superiority of the spiral bSSFP sequences over the radial bSSFP sequence in real-time cardiac function MRI. We ultimately hope to propel the clinical adoption of the spiral bSSFP sequences with this study.

Chapter 4

Spiral Parallel Imaging Techniques and Real-Time Velum Imaging

4.1 Introduction

Velopharyngeal insufficiency (VPI) is the incomplete closure of the port bordered by the soft palate and the posterior and lateral pharyngeal walls. VPI is most commonly seen in children who have had a cleft palate repair, a submucous cleft, or as a complication from an adenoidectomy. There is no gold standard for the instrumental diagnosis of VPI. Nasal endoscopy and multi-planar video fluoroscopy are the most common diagnostic modalities employed in children with suspected VPI. Drawbacks to nasal endoscopy include poor patient tolerance in very young children. Fluoroscopy also requires significant patient cooperation and leads to radiation exposure. The current surgery procedure for the cleft palate repair only sews the cleft palate without much considerations on the velum function during speech so that a second surgery aiming to cure the resulting VPI is usually required. Therefore, velum muscle modeling is important for the guidance of an improved procedure and is currently under investigation.

Magnetic resonance imaging (MRI) has been studied for evaluating and modeling VPI because it provides the ability to analyze the anatomic detail of the oropharynx in multiple planes without radiation exposure. The MRI of the velum before and after surgery has been performed for the evaluation of occult submucous cleft palate with an oblique coronal slice [40]. Velum and nasopharyngeal wall modeling based on MRI and CT data has also been developed for the understanding of oral and nasopharyngeal functions during speech [41]. However, in these methods static MR images were acquired with a relatively long scan time, so that little dynamic information could be obtained during speech, and hence the evaluation and modeling was not comprehensive and might be inaccurate. Dynamic MRI using various techniques to reduce the scan time has been developed and applied during speech [42–45]. In [42], the dynamic MR image series of one sagittal slice with 1.87 mm spatial resolution were acquired during speech and swallowing at 21 fps using a real-time spiral FLASH sequence. A subsequent investigation increased the temporal resolution to 100 fps [43] by using a dynamic model to reduce the degrees of freedom of the tongue movement during speech. The increase in temporal resolution is dramatic; however, the effectiveness of the dynamic model in capturing the entire tongue and velum movements in a very complicated speech is not fully validated. In [44], a golden-ratio spiral view order was used to retrospectively select temporal resolution in real-time speech MRI. However, the view sharing reconstruction can bring in temporal blurring. In [45], real-time MRI of speaking was acquired at a temporal resolution of 33 ms using undersampled radial FLASH with nonlinear inverse reconstruction. A midsagittal and coronal plane were acquired separately and quantitative image analysis was performed to study the deformation of the vocal tract. In our study, we will focus on velum movements during speech for VPI evaluation and modeling. In order to acquire sufficient dynamic information of the velum during speech, we aim to simultaneously acquire two slices of the velum with sagittal and oblique coronal views.

As spiral trajectories are more time-efficient in data acquisition than Cartesian trajectories, we can use a real-time spiral GRE sequence for this application to improve the spatial and/or temporal resolution and coverage. As the requirements for temporal and spatial resolution and SNR are very demanding, spatial parallel imaging techniques using multiple receiver coils and the temporal parallel imaging techniques exploiting the temporal redundancy in an image series are also required in combination with the spiral trajectory for a further reduction of the scan time. In addition, the $B0$ field inhomogeneity resulting from the air-tissue boundary around the velum is very severe in this application and image blurring resulting from this needs to be corrected.

With high resolution dynamic velum image series acquired during a given pronunciation or movement, a more distinctive visual diagnosis and quantitative analysis of VPI becomes possible. In addition, a muscle movement model of the velopharyngeal sphincter can be validated. The diagnostic study and muscle modeling are mainly performed by our collaborators and thus are beyond the scope of this dissertation.

In the following sections we will focus on general spiral parallel imaging techniques and their application in real-time velum imaging. In the theory section spiral parallel imaging techniques and their combination with off-resonance correction will be introduced. In the method section the sequence design and implementation and the post-processing will be described. In the result section the experimental results will be presented. Finally the conclusion and some further directions will be given.

4.2 Theory

4.2.1 Spatial Parallel Imaging

Due to the non-Cartesian sampling pattern of the spiral trajectory, the direct application of the Cartesian spatial parallel imaging techniques represented by SENSE and GRAPPA is impractical. Various methods have been developed to tackle this problem either by using the coil sensitivity map and applying an iterative algorithm to achieve an optimized image (iterative SENSE [46]) or by using auto-calibrated information to fill the undersampled k-space (SPIRiT [47]). The auto-calibrated parallel imaging techniques are often preferred in dynamic MRI applications because it is usually very difficult to accurately estimate the coil sensitivity map, especially when the map can vary with time due to the chest movements in certain applications. Although in this real-time velum imaging application the coil sensitivity map estimation is less difficult as the head and neck coils are fixed, we still choose the newly developed auto-calibrated method SPIRiT due to its simplicity and robustness to all k-space sampling patterns without a comprehensive argument about its superiority.

In SPIRiT, for a non-Cartesian sampling pattern, the image reconstruction is done with a minimization problem described by

$$\text{arg}\min_{x}\{\|Dx - y\|_2^2 + \lambda\|(G - I)x\|_2^2\} \tag{4.1}$$

in which x is the reconstructed image, D is the NUFFT data encoding matrix to get the Fourier transform of the image at each non-Cartesian sampling position [48], G is a series of convolution operators that convolve the entire k-space with the appropriate calibration kernels, and I is the identity matrix. The second term represents the self-consistency of the k-space data from multiple receiver coils expressed in the image domain.

The calibration is usually performed with the fully-sampled center k-space data. In a dynamic imaging application using the undersampled spiral trajectory at each frame, this fully-sampled data can be either acquired by combining the data from neighboring frames or by using a dual variable density spiral trajectory in which the center k-space is fully-sampled. However, when the undersampling ratio becomes very large (4x or 6x), the former suffers from severe data inconsistency due to the movements of the subject during several neighboring frames while the latter requires a very high oversampling ratio in the original trajectory design and thus greatly reduces the data acquisition efficiency and limits the spatial resolution. Since two single-shot spiral scans are acquired before data acquisition for the low resolution field map, they can be also used to get the calibration kernel. Even though the single-shot spiral data is contaminated with off-resonance effects, we will demonstrate that the off-resonance will not affect the calibration process and the corresponding self-consistency property if the kernel is relatively small and the k-space data inside the kernel is temporally adjacent.

The self-consistency requirement can be expressed as

$$S_n(k_x, k_y) = \sum_{\Delta k_x, \Delta k_y, p} g_n(\Delta k_x, \Delta k_y, p) S_p(k_x + \Delta k_x, k_y + \Delta k_y) \tag{4.2}$$

in which S is the k-space data with n and p indicating different coils and g is the convolution kernel. If we ignore the gridding operation for now and assume S is the spiral k-space data including the off-resonance effects, we can replace S with the corresponding signal equations and have

$$\begin{aligned} &\int_{x,y} m(x,y) C_n(x,y) e^{i\Delta\omega(x,y)t} e^{i2\pi(k_x x + k_y y)} dxdy \\ &= \sum_{\Delta k_x, \Delta k_y, p} g_n(\Delta k_x, \Delta k_y, p) \int_{x,y} m(x,y) C_p(x,y) e^{i\Delta\omega(x,y)t'} e^{i2\pi((k_x+\Delta k_x)x + (k_y+\Delta k_y)y)} dxdy \end{aligned} \tag{4.3}$$

in which $C(x, y)$ is the coil sensitivity. t' in the above equation is a function of Δk_x and Δk_y, since the k-space data inside the range of the kernel centered at $(k_x,\ k_y)$ is acquired at different times. However, if the kernel is small, which is usually true as we often use $7*7$ kernel size and the k-space data inside the kernel is temporally adjacent, we can assume $t' = t$ and therefore the above equation can be simplified into

$$C_n(x, y) = \sum_{\Delta k_x, \Delta k_y, p} g_n(\Delta k_x, \Delta k_y, p) C_p(x, y) e^{i2\pi(\Delta k_x x + \Delta k_y y)} \tag{4.4}$$

which is the basic equation of all the auto-calibrated parallel imaging methods [49]. Therefore, even with the off-resonance contaminated k-space data, the self-consistency requirement can still be satisfied and the kernel value does not change as long as the phase term due to off-resonance has little variation inside the kernel compared with the center k-space point of the kernel. In addition, since the gridding kernel is even smaller, the phase variation inside the kernel is also small and therefore the gridding will not affect this self-consistency property, either. Therefore, in the calibration step using the single-shot spiral, although the k-space data inside the kernel may not be temporally adjacent, the small size of the kernel can limit the phase variations. For the multi-shot undersampled spiral data acquisition, the k-space data inside the kernel is always temporally adjacent when the interleaf number is larger than the kernel size as long as each interleaf of the spiral trajectory starts at the center of k-space and traverses to the edge with the same speed.

In the gridding operation for a general fully-sampled spiral reconstruction, oversampling is often used to compensate for gridding error due to the finite kernel size. In addition, if there is remaining signal outside the selected FOV, this oversampling can reduce aliasing by supporting a larger FOV. In the SPIRiT recon, we believe that the oversampling is even more important in terms of reducing the aliasing and gridding error, because small errors can accumulate during each iterative step. Figure 4.1 shows reconstructed images without and with oversampling for the same data set. In the left image, the signal from the neck outside the FOV causes severe aliasing artifacts that appear as stripes in the lower part of the image. These are mostly eliminated in the right image with 1.5x oversampling along the vertical direction. Oversampling along the horizontal direction is not performed for a faster computation since the horizontal FOV is large enough for the entire head. To perform oversampling during the SPIRiT recon, we just need to enlarge the image matrix and the k-space trajectory by the oversampling

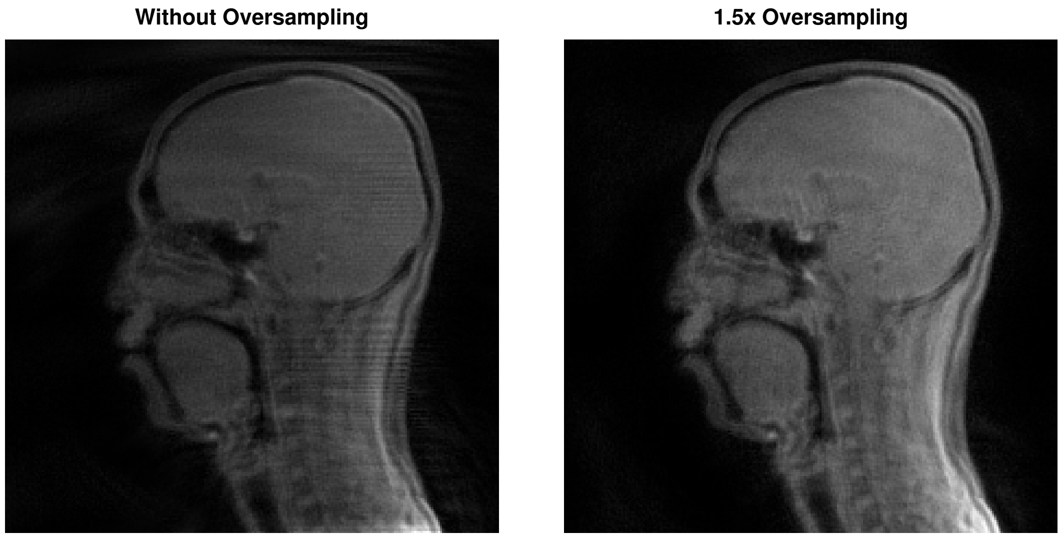

Figure 4.1: *SPIRiT reconstructed images without and with 1.5x oversampling along the vertical direction. The horizontal stripes in the left image are mostly eliminated in the right image with oversampling.*

ratio.

4.2.2 Temporal Parallel Imaging

In an image series for most dynamic applications, temporal redundancy exists because the neighboring images are highly correlated. Therefore, undersampling is often used to reduce the data acquisition time for each frame and thus to increase the temporal and/or spatial resolution. A very simple but efficient way to exploit this redundancy is to directly use the k-space data acquired from neighboring frames to fill the corresponding missing k-space data of the current frame, which is known as view sharing. View sharing methods include the sliding window (SW) method, which directly uses the previously acquired k-space data, and the SLAM method [50], which uses linear interpolation of the closest neighboring frames to estimate the missing k-space data. This type of method is robust in terms of reducing spatial aliasing when the undersampling ratio is small and the dynamic process is not very fast; however, it suffers from severe temporal blurring and motion-induced ghost artifacts with very rapid movement of the imaged subject.

The emergence of compressed sensing theory [51, 52] brings in the concept of sparsity to characterize redundancy. With an appropriate "sparsifying" transform, which can result in many near zero components in the transformed domain, the reconstruction of undersampled data can be achieved via the minimization problem

$$\arg\min_x \{\|Dx - y\|_2^2 + \lambda \|\Psi x\|_1\} \tag{4.5}$$

where D is the data encoding matrix and Ψ is the sparsifying transform. According to compressed sensing theory, an incoherent encoding matrix is required and the $l1$ norm of the transformed domain is minimized rather than the $l2$ norm to get the sparsest result. While there are many controversial opinions on the coherency of different sampling patterns [53, 54], we ignore those arguments and assume the undersampled spiral sampling pattern is a suitable choice here, since the variable density spiral trajectory has a very uniformly distributed aliasing pattern to reduce the coherence level. The sparsity transforms for a dynamic image series include the image differences between neighboring frames, the temporal frequency, the Karhunen-Loève (KL) transform of the temporal frequency [55, 56] and the wavelet transform along the time axis. Again it is highly debatable which transform is preferable; probably the idea of having a best sparsifying transform to exploit temporal redundancy in all dynamic applications is untenable due to the complexity and variability of each dynamic phenomenon.

In real-time velum imaging, since the tongue and velum movements are non-periodic, the Fourier transform along the time axis cannot result in a significant improvement in sparsity level and thus using this constraint in Eq. (4.5) can lead to the loss of some important frequency information. However, since most parts of the head are static and the tongue and velum movements are continuous in time during speech, the image differences between neighboring frames are often very sparse. Therefore, we can use the temporal difference as the sparsifying transform. In addition, since the dynamic level in the image series is spatially variant as some areas inside the FOV are almost static while other areas may experience very rapid change [57, 62], it is less efficient to minimize the image differences with a spatially invariant constraint coefficient λ. Assuming we can estimate the local dynamic level, we can spatially vary the constraint coefficient by using a larger coefficient for the less dynamic areas and a smaller coefficient for the more dynamic areas to punish temporal variation in less dynamic areas more.

The spatial variation of λ is given as

$$\lambda(\mathbf{r}) = \frac{\lambda}{Var(\mathbf{r})/\mathsf{min}(Var(\mathbf{r}))} \tag{4.6}$$

in which $Var(\mathbf{r})$ is the estimated local variance achieved from a SLAM reconstruction or a spatially invariant temporal difference constrained reconstruction. In practice, if the undersampling ratio is larger than 4, the SLAM reconstruction will have very severe ghost artifacts leading to erroneous local variance estimation and therefore the spatially invariant temporal constraint reconstruction is used at the cost of increased computation time.

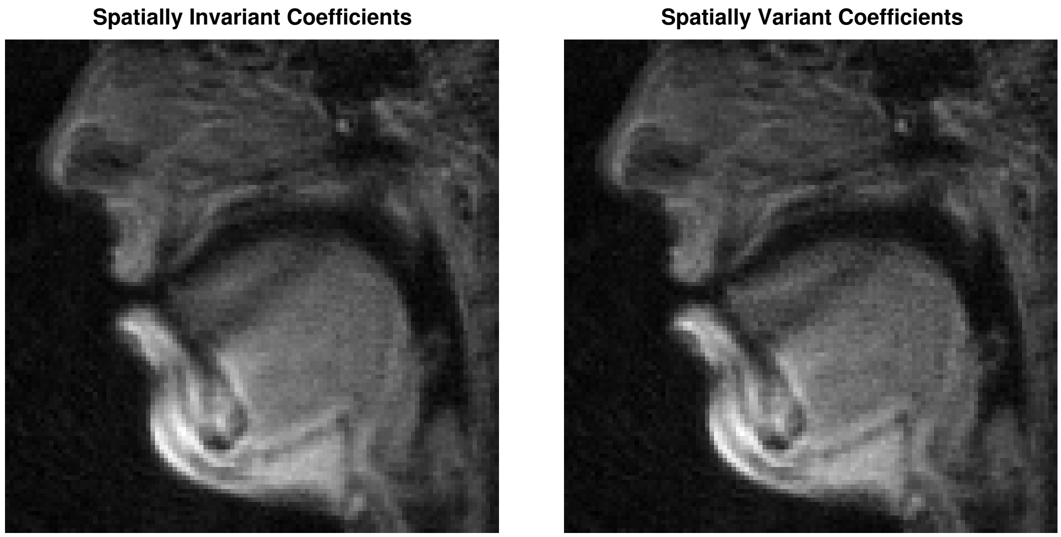

Figure 4.2: *Images reconstructed with temporal difference constraint using spatially invariant and variant constraint coefficients.*

Figure 4.2 shows reconstructed images with spatially invariant and variant constraint coefficients. The λ used in the spatially invariant constraint coefficient weighted reconstruction is 10 times that of the λ in the spatially variant constraint coefficient weighted reconstruction to balance the overall temporal constraint level. We can see that the temporal blurring is reduced with the spatially variant constraint coefficient as it relies more on the acquired k-space data to get the image in the more dynamic area and relies more on the temporal constraint to get the image in the less dynamic area.

4.2.3 Combined Spatial and Temporal Parallel Imaging

Based on compressed sensing theory, the total variation along each direction of one frame is also sparse for most medical images; therefore, it can be put into the minimization problem for a higher SNR. However, the corresponding constraint coefficient needs to be selected carefully to avoid over-smoothing of the image, since total variation tends to smear the boundaries between different image regions. The selection is usually performed by using a range of coefficients to do the reconstruction and visually selecting an appropriate coefficient. Combining the spatial and temporal parallel imaging techniques, we arrive at the minimization problem given as

$$\arg\min_{x}\{\|Dx(\mathbf{r},t)-y\|_2^2+\beta\|(G-I)x(\mathbf{r},t)\|_2^2+\lambda(\mathbf{r})\|\nabla_t x(\mathbf{r},t)\|_1+\gamma\|\nabla_{\mathbf{r}}x(\mathbf{r},t)\|_1\} \tag{4.7}$$

in which β, $\lambda(\mathbf{r})$ and γ represent the constraint coefficients for spatial parallelism, temporal differences and total variation. By exploiting these constraints in combination, the undersampling ratio can be as high as $6x$ without severe aliasing.

The minimization of this problem is generally solved using a non-linear conjugate gradient method [52]. The SLAM reconstructed image series is used as the starting point for this problem since this image series has minimal spatial aliasing, so that the number of required iterations can be decreased.

4.2.4 Off-Resonance Correction

During speech, since the air-tissue boundary is continually changing with tongue and velum movements, the field map also changes with time. Therefore, we need to update the field map for each frame to deblur the entire image series. In fact, as off-resonance does not affect the self-consistency property of the k-space data and the temporal differences if the field map variation is small between neighboring frames, we can do the deblurring after unaliasing with Eq. (4.7), assuming the resulting $x(\mathbf{r},t)$ is the blurred image series.

Since we will acquire the low-resolution field map before the data acquisition, we can use it to delimit the search range of a high-resolution field map using the semi-automatic method introduced in Chapter 2 for every frame, assuming the temporal variation of the field map is within the search range. Fast conjugate phase reconstruction based on a Chebyshev approximation can be performed afterwards for each frame with the time-invariant concomitant gradient field.

Alternatively, we also developed a method to do deblurring during unaliasing by directly modifying the data encoding matrix D in Eq. (4.7) to incorporate the off-resonance information, which is given as

$$D(\mathbf{k}(t'), t)x = \int_{\mathbf{r}} x(\mathbf{r}, t) e^{i\Delta\omega(\mathbf{r})t'} e^{i\phi_c(\Delta\omega_c(\mathbf{r}), t')} e^{-i2\pi\mathbf{k}(t')\cdot\mathbf{r}} d\mathbf{r} \tag{4.8}$$

in which $\mathbf{k}(t')$ is the k-space location. The field map $\omega(\mathbf{r})$ can be determined using the aforementioned semi-automatic method. However, as the unaliased image is unavailable for each frame, we have to use the temporally blurred image series reconstructed using SLAM to get this map assuming the field map changes at a slower rate than the dynamic image series. With the off-resonance information, it is actually very impractical to calculate the phase for each k-space point in equation (4.8) with different acquisition time t'; therefore, a time segmented method is used to approximate the field map phase by assuming the data is acquired at the same time in each segment. In addition, the concomitant gradient induced phase is omitted since it is relatively small and also impractical to calculate.

Figure 4.3 shows reconstructed images without deblurring, with deblurring during unaliasing and with deblurring after unaliasing. In this experiment the undersampling ratio is 2x so that only the spatial parallel imaging technique is

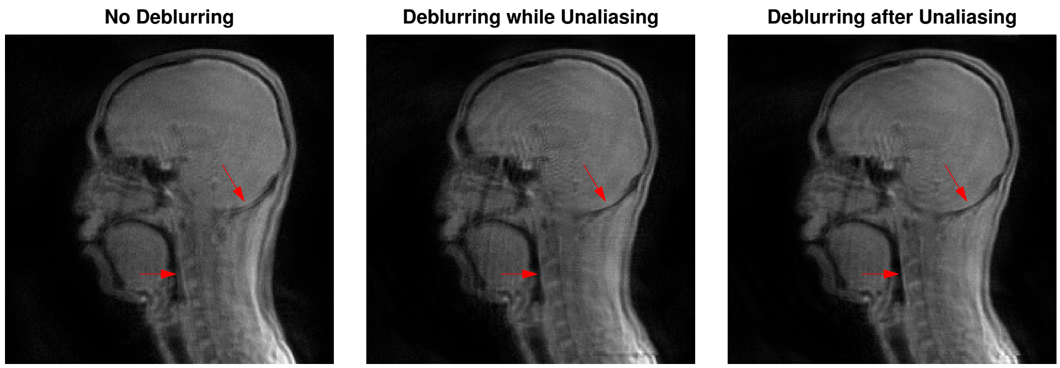

Figure 4.3: *Reconstructed images using the spatial parallel technique without deblurring, with deblurring during unaliasing and with debluring after unaliasing.*

applied for simplification due to the very high computational load of the segmentation process. It is demonstrated that the deblurring is required to get a cleaner airway and the velum and skull boundaries as indicated by the arrows. Comparing the two deblurring methods, we see that deblurring after unaliasing is more effective, since the field map is updated for every frame and the concomitant gradient field is also considered. In addition, the deblurring step after unaliasing only adds a limited amount of computation, while the deblurring during unaliasing requires approximately segment-number-multiplied computation load. Therefore, deblurring after the unaliasing is preferred in our reconstruction. The effectiveness of this deblurring is further demonstrated in Fig. 4.4, in which the undersampling ratio is 6x and Eq. (4.7) is performed. The velum boundary is sharpened as indicated by the arrow.

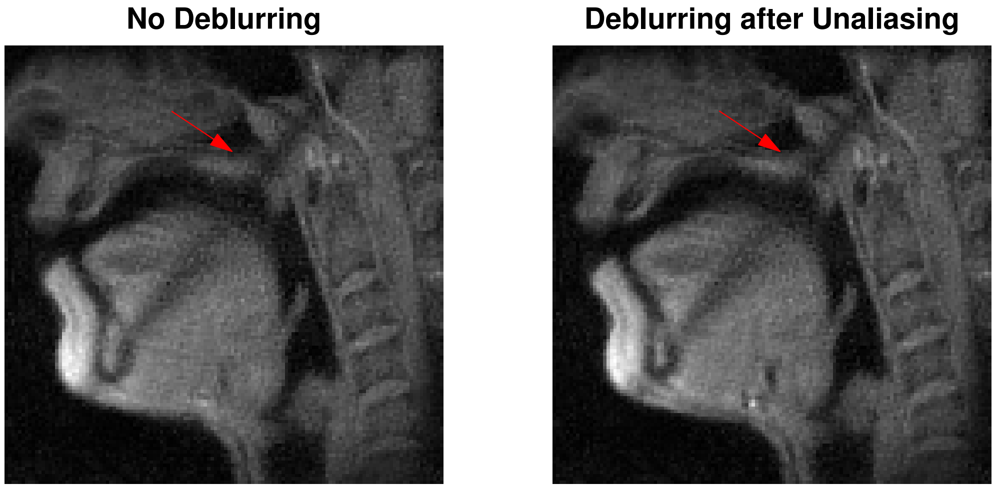

Figure 4.4: *Reconstructed images using combined spatial and temporal parallel techniques without (left) and with (right) deblurring after unaliasing.*

4.3 Method

4.3.1 Sequence Design

To reduce scan time, a fast gradient-echo type of sequence is used. For this application we choose a spiral steady state free precession (FISP, GRASS, or FFE) sequence, because it can provide higher SNR for the T1 and T2 values of the velum compared with a spoiled gradient echo sequence and it is more robust to severe off-resonance effects, especially in air-tissue boundary, compared with the balanced SSFP sequence. A flip angle of 20° is used to approximately maximize the SNR for the velum. A low resolution field map is acquired before data acquisition for semi-automatic high resolution map estimation.

For the spiral trajectory, we use a linear variable density readout design. The fully sampled trajectory has 18 interleaves with 3.6 ms readout per interleaf.

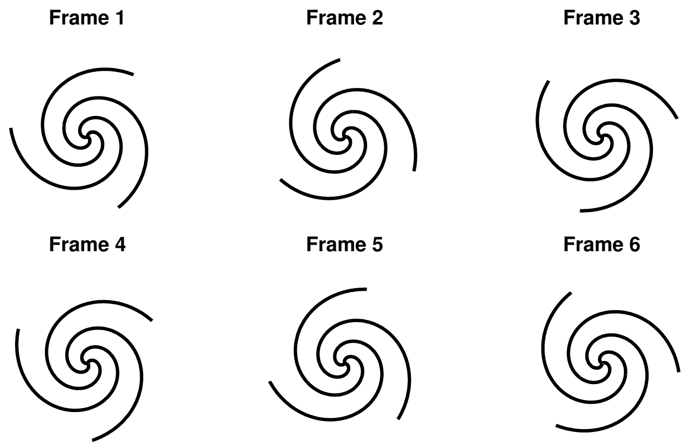

Figure 4.5: *The spiral trajectories for the real-time velum imaging of* 6 *frames with 6x undersampling ratio.*

The resulting minimum TR is 6.96 ms and TE is 0.78 ms. 6x undersampling is used so that the spiral k-space data of 3 interleaves is used to reconstruct each frame. We use an odd number of interleaves per frame to avoid information redundancy with conjugate k-space data and the 3 interleaves are 120 ° apart from each other for uniform coverage of the k-space. Between neighboring frames, the 3 interleaves are rotated with an angle calculated using the bit-reversed table of the undersampling ratio. Repetitive trajectories are used for the entire image series with a period of the undersampling ratio, so that the SLAM recon can be performed for the starting image series in Eq. (4.7). Figure 4.5 shows the spiral interleaves for every 6 frames. The rotation angles relative to the first frame are respectively 0, 80 °, 40 °, 20 °, 100 ° and 60 °.

4.3.2 Experiment Setup

For a comprehensive evaluation of the velum movements, dynamic image series of two 2D slices were simultaneously acquired, with one mid-sagittal slice and one oblique slice along the velum movement direction and perpendicular to the sagittal slice as indicated in Fig. 4.6. Spatial saturation pulses were applied for a reduced FOV as also shown in Fig. 4.6 to achieve higher spatial resolution. However, instead of applying the spatial saturation pulses for every TR and every slice, we apply these pulses for every frame and share the saturated bands between the two slices to reduce the scan time and increase the temporal resolution. The sequence diagram is shown in Fig. 4.7. In the actual experiment, the first several frames are often omitted to avoid the signal inconsistency before the steady state is reached.

The experiments were performed on a Siemens Avanto 1.5 T scanner equipped with multiple channel head and neck coils. Healthy volunteers with informed consent were scanned while being asked by the language pathologist to repeat a specific sound or action corresponding to a specific velum movement. In the current protocol, we use 1.2x1.2 mm^2 resolution with 150 mm FOV and 8 mm slice thickness and can achieve 20 frames-per-second (fps) temporal resolution. The dynamic image series are then reconstructed offline with Matlab using the algorithm introduced before.

4.3.3 Dark Band Correction

Since we interleave the spiral acquisitions of these two non-parallel slices, the area of intersection will have a lower signal intensity due to the shortened effective

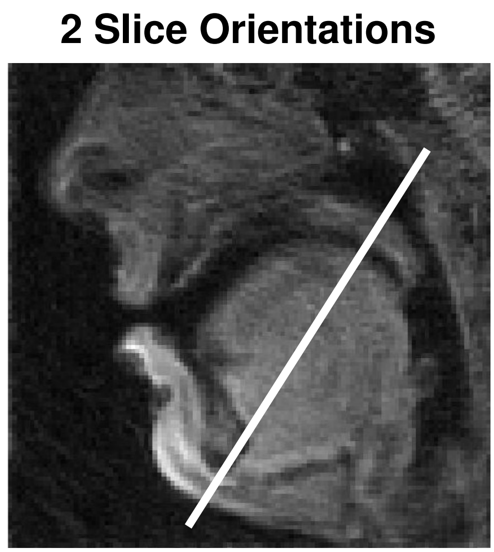

Figure 4.6: *This figure shows the two slice orientations in this study. The white band indicates the orientation of the second slice, which is perpendicular to the mid-sagittal slice shown.*

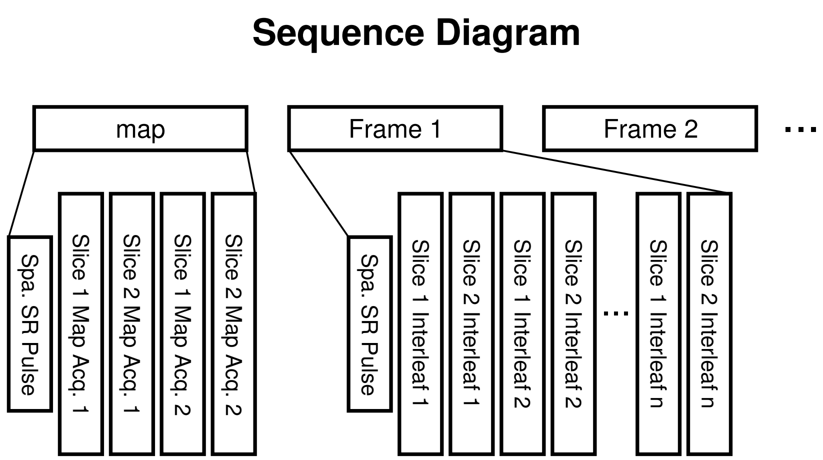

Figure 4.7: *The sequence diagram for the real-time velum imaging.*

TR and behave as a dark band. In theory, if we can get the local T1 and T2 information, the decay ratio of the dark band signal can be calculated with a given set of sequence parameters. However, this would require additional scans to acquire the T1 and T2 maps. In practice, we develop a simple correction algorithm to compensate for the dark band after image reconstruction assuming the signal decay ratio within the dark band does not change very rapidly at different locations.

To correct for the signal decay, first the location and width of the dark band are calculated with the orientation and thickness of the two slices. Then the dark band is segmented into several small blocks, assuming each block has a unique signal decay ratio which can be estimated by dividing the mean image intensity of the neighboring blocks outside the dark band by the mean image intensity of this block within the dark band. In addition, to account for the fact that the slice profile is not a strict rectangle function with the truncated-sinc RF pulses, we estimate a different signal decay ratio within the edge regions of the dark band using the same method.

4.4 Results

4.4.1 Dark Band Correction

Figure 4.8 shows images before and after the dark band correction. The signal decay within the band is mostly compensated and the boundaries of the dark band are much less obvious after the correction.

Figure 4.9 shows 6 consecutive images of the two slices indicating the velum

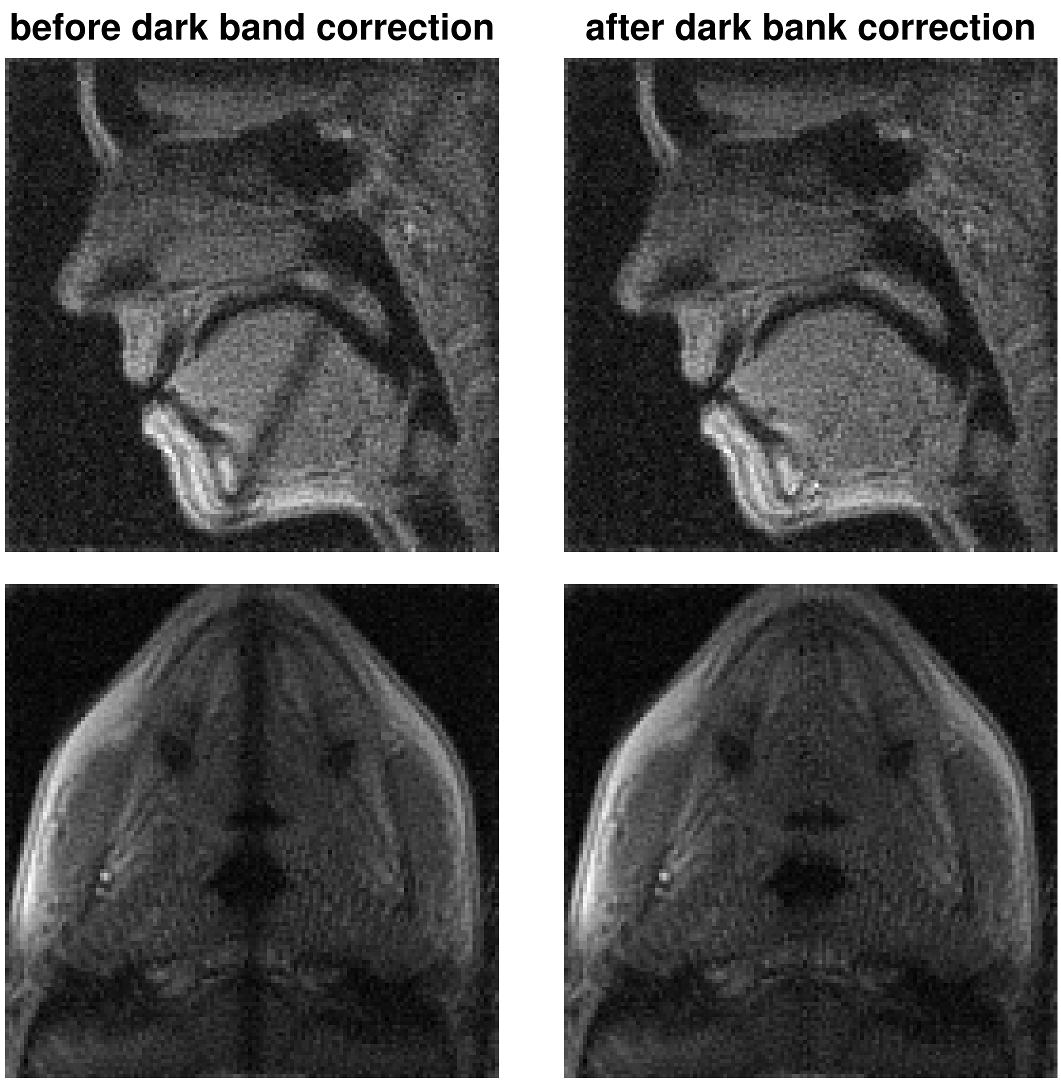

Figure 4.8: 6 *Images before and after dark band correction.*

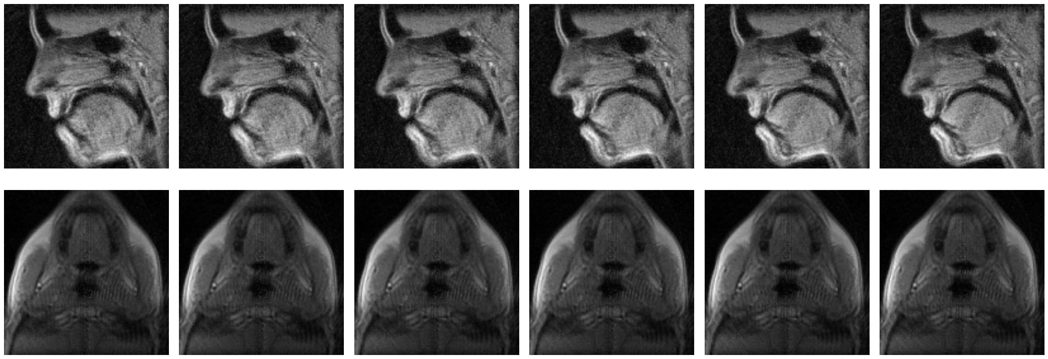

Figure 4.9: 6 *consecutive images of two slices indicating the velum movements during speech in a healthy volunteer study.*

movements during speech. The velum moves towards the tongue to enlarge the nasal airway during this sound. The nasal and oral pathway areas can be roughly calculated from the second slice images. This demonstrates the feasibility of using MR real-time velum imaging as a new diagnostic tool for VPI and for facilitating dynamic velum muscle modeling to explore the mechanism of VPI.

4.5 Discussion

In this chapter we introduced spiral spatial and temporal parallel imaging techniques for undersampled data reconstruction and their application to real-time velum imaging during speech for VPI evaluation and modeling.

We used the SPIRiT method to exploit the spatial redundancy from multiple receiver coils with oversampling to reduce the gridding error and support a larger FOV. We also demonstrated that off-resonance effects do not affect the self-consistency property of the k-space data, so that the center k-space data acquired for low resolution field map can be also used for the SPIRiT kernel training. To exploit the temporal redundancy of a dynamic image series we minimized the temporal differences between neighboring frames with spatially variant constraint coefficients. In addition, the total variation of each frame was added as an addition constraint based on compressed sensing theory. Wavelet analysis of each frame can also be minimized for further reduction of aliasing; however, the computational load will be greatly increased and the reconstruction time is too long to be practical. In fact, even with the current algorithm, the reconstruction is very slow as parallel computation and GPU-based algorithms are not realized in the current reconstruction. Online reconstruction is not implemented, either. Therefore, a future direction will be the acceleration of the reconstruction and the online implementation.

We developed an imaging protocol for real-time velum imaging during speech to simultaneously acquire two slices to capture the dynamic information of the velum. We used a spiral SSFP/GRASS sequence for higher SNR and fewer off-resonance artifacts. Spatial saturation pulses are used for a reduced FOV and are shared by the two slices. In fact, the steady state can be perturbed by the slightly lengthened effective TR for certain spiral interleaves due to the saturation pulses, but the contrast between the air and tissue is large enough so that the contrast mechanism due to different signal pathways is not a major concern in this application, since we only want to depict the velum movements.

With high resolution dynamic image series of the velum, we can do the visual and quantitative analysis of velum movement during a specific speech pattern. The velum muscle model can be also validated with the image series.

Chapter 5

Cartesian Kalman Filter Techniques and their Application to Real-Time Cardiac Function MRI

5.1 Introduction

As introduced before, dynamic MRI is becoming more popular with the recent development of both MRI hardware and software. Short scan time is typically needed to reduce motion artifacts. Even though the spiral trajectory is inherently a faster k-space sampling scheme, the Cartesian trajectory is still dominant in clinical adoption due to its simplicity and robustness. Similar to spiral spatial and temporal parallel imaging techniques, redundancy in the acquired Cartesian k-space data and/or the dynamic image series can be exploited so that less k-space data is required for the given spatial and temporal resolution. Spatial parallel imaging techniques including SENSE and GRAPPA for the Cartesian trajectory have been widely used on scanners to effectively reduce scan time without degrading image quality. To exploit temporal redundancy, view sharing methods including SW and SLAM can be also used for the Cartesian trajectory as in the spiral trajectory mentioned before. However, they can also bring in temporal blurring and more distinct motion induced ghost artifacts when the movements are very rapid.

Instead of exploiting the redundancy in the time domain, other techniques apply a 1D Fourier transform along the time direction to exploit the redundancy in the frequency domain and then use advanced reconstruction methods to recover the image series. These techniques include UNFOLD [57], kt-BLAST [58] and kt-FOCUSS [59], and they show advantages over view sharing techniques in reducing aliasing and temporal blurring. Another category includes many reduced FOV (rFOV) methods [60–62], which take advantage of the fact that some parts in the FOV are relatively static in a dynamic image series so that the number of required k-space lines to update an individual image can be reduced. One representative method called Noquist [62] can effectively reconstruct the image series without residual artifacts from undersampled k-space data by decomposing the image and the corresponding Fourier transform matrix into dynamic and static parts and solving the resulting inverse problem with greatly reduced degrees of freedom, because the static part of the image series stays the same throughout the image series and requires much less data to reconstruct. However, these two types of methods often use retrospective reconstruction, which inhibits their adoption in many clinical applications in which real-time reconstruction is required, such as real-time catheter tracking and cardiac stress function studies. Furthermore, these techniques are not always robust; for example, in real-time cardiac imaging, the effectiveness of these methods can be impaired by respiratory motion during free breathing [63].

Recent techniques based on compressed sensing, including the aforementioned kt-FOCUSS and temporally constrained reconstruction methods [64], which exploit sparsity in the time and/or frequency domain, have gained attention. However, a major disadvantage of these methods is the long reconstruction time due to the iterative reconstruction, so that physicians cannot get the reconstructed images for rapid feedback during the scan. Furthermore, the nonlinear characteristics of these techniques make it difficult to predict and evaluate the noise in the images compared with linear methods.

The Kalman filter, a widely used method in many engineering fields including real-time object tracking, can also exploit the temporal redundancy in a time series by describing the dynamic problem with a time-evolving state model and rapidly estimating the current state using a real-time linear filtering process. Therefore, it is plausible to use this method in dynamic MRI for real-time imaging and real-time reconstruction. The original adoption of the Kalman filter in dynamic MRI was proposed by Sümbül et al. [20, 21]. However, this method was confined to non-Cartesian k-space trajectories because of a limitation intrinsic to the model used in that study. In this dissertation we adapt the Kalman filter model to make it available for the more widely used Cartesian trajectory.

Spatial and temporal redundancy can be exploited in combination to more effectively reduce the scan time. Previous spatiotemporal acceleration approaches include TSENSE [65] and TGRAPPA [66], which mainly rely on spatial parallelism but improve the results with the temporal information; kt-SENSE [58], which is an expansion of kt-BLAST that incorporates coil sensitivity into the model; and PINOT [67], which combines the SPACE-RIP parallel imaging method [68] and the Noquist method. In this dissertation we also combine the Kalman filter model with spatial parallel imaging techniques. If reliable coil sensitivity maps can be acquired, they can simply be incorporated into the model as in kt-SENSE and the non-Cartesian Kalman filter combined with SENSE [20]; however, since accurate coil sensitivity maps in many dynamic problems are difficult to achieve, we also developed a method that combines the Kalman filter with TGRAPPA to bypass the coil sensitivity estimation step.

In the following sections, we will first introduce the implementation of the Kalman filter in Cartesian dynamic MRI, including the combination with parallel imaging techniques. Next, we focus on non-gated real-time cardiac imaging to study the performance of the Kalman filter model by both simulation and experiment. Finally, we will discuss our results and possible extensions.

5.2 Theory

In general, a Kalman filter model is composed of a system model that describes the relationships among the time-evolving states and a measurement model that describes the measurement of the state at a given time. Usually the current measurement at a given time alone is not sufficient to obtain an accurate estimate of the current state. The key to the Kalman filter is to use all previous measurements and the relationship between states as described by the system model to estimate the current state. Furthermore, the estimation process is recursive, so there is no need to store past measurements for the purpose of computing present estimates. Thus, the process can be very fast and memory efficient. The general model of a Kalman filter is given as follows [69]

$$\begin{aligned} \mathbf{x}_k &= \mathbf{\Phi}_{k-1}\mathbf{x}_{k-1} + \omega_{k-1}, \qquad \omega_k \sim N(\mathbf{0}, \mathbf{Q}_k) \\ \mathbf{z}_k &= \mathbf{H}_k\mathbf{x}_k + \nu_k, \qquad \nu_k \sim N(\mathbf{0}, \mathbf{R}_k) \end{aligned} \tag{5.1}$$

where $\mathbf{x}_k$ is the system state in a vector form, $\mathbf{\Phi}_k$ is the state transition matrix, ω_k is the system noise vector assumed to have a zero-mean Gaussian distribution with covariance matrix $\mathbf{Q}_k$, $\mathbf{H}_k$ and $\mathbf{z}_k$ are the measurement matrix and the corresponding measurement data, and ν_k is the measurement noise also assumed to have a zero-mean Gaussian distribution with covariance matrix $\mathbf{R}_k$. Given the appropriate initial conditions and assuming ω_k and ν_j are independent, we can get the state estimate $\hat{\mathbf{x}}_k$ by a prediction-correction process described as

$$\begin{aligned} \hat{\mathbf{x}}_k^- &= \mathbf{\Phi}_{k-1}\hat{\mathbf{x}}_{k-1}^+ \\ \hat{\mathbf{x}}_k^+ &= \hat{\mathbf{x}}_k^- + \mathbf{K}_k[\mathbf{z}_k - \mathbf{H}_k\hat{\mathbf{x}}_k^-] \end{aligned} \tag{5.2}$$

where the $-$ and $+$ refer to the predicted and corrected state estimates and $\mathbf{K}_k$ is the Kalman gain matrix calculated from $\mathbf{H}_k$, $\mathbf{Q}_k$, $\mathbf{R}_k$ and $\mathbf{\Phi}_k$ [69]. The general equations to calculate $\mathbf{K}_k$ are omitted here for brevity, as they will be discussed below in the model implementation section.

If we want to directly apply the Kalman filter model to a dynamic MRI application acquiring a 2D image series, the state to be estimated at each time point k is one individual image from the image series and the corresponding measurement is the acquired k-space data, where the measurement matrix is the 2D Fourier transform in matrix form. One major obstacle here is the size of the vectors and matrices. For an individual N by N image, the dimension of the state vector is $N^2 * 1$ and the corresponding matrix is $N^2 * N^2$, which is generally too large to handle for a typical value of N. In Sümbül's paper [20], a diagonalization assumption is made for $\mathbf{Q}_k$, $\mathbf{R}_k$ and $\mathbf{H}_k^T\mathbf{H}_k$ so that the prediction-correction process can be performed on a pixel-by-pixel basis to bypass the matrix multiplication and inversion steps in calculating $\mathbf{K}_k$. The diagonalization of $\mathbf{Q}_k$ and $\mathbf{R}_k$ can still be applied for Cartesian trajectories, because $\mathbf{Q}_k$ reflects statistical properties of the dynamic image series that are independent from the data acquisition, and the diagonalization of $\mathbf{R}_k$ is intrinsic due to the whiteness of the measurement noise.

However, the diagonal simplification for $\mathbf{H}_k^T\mathbf{H}_k$ is only possible for a non-Cartesian k-space trajectory such as a spiral trajectory. Assuming $\mathbf{H}_k$ is the undersampled 2D Fourier transform matrix connecting the image domain and the k-space domain with a matrix-vector multiplication, the off-diagonal terms of $\mathbf{H}_k^T\mathbf{H}_k$ are determined by the aliasing pattern as displayed in the point spread function. For a spiral trajectory, the aliasing is diffuse and the side lobes of the point spread function are more evenly distributed; therefore, each single off-diagonal term is very small compared to the diagonal term and can be ignored without nullifying the model. However, for a Cartesian k-space trajectory, the aliasing pattern is generally very conspicuous as shown by separate peaks in the point spread function; therefore, the off-diagonal term of $\mathbf{H}_k^T\mathbf{H}_k$ cannot be ignored. Without the diagonalization of $\mathbf{H}_k^T\mathbf{H}_k$, the direct implementation of the Kalman filter is impractical since the matrix calculation process can be extremely complicated and will greatly increase the reconstruction time. However, in an undersampled 2D Cartesian k-space measurement, undersampling usually only happens in the phase encoding direction and k-space is often fully sampled or even over sampled in the readout direction. Therefore, we can first apply a direct 1D Fourier transform along the readout direction and then use the Kalman filter for the reconstruction along the phase encoding direction for each readout pixel. By doing that, for the same N by N image, we now have N Kalman filter models which can be calculated in parallel, and for each model, the dimension of the state vector becomes N and the matrix size becomes reasonable. Furthermore, since we have already transformed into the image domain along the readout direction before the Kalman filter model implementation, in many cases we need fewer than N Kalman filter models to cover the ROI along the readout direction, because portions of the object may not experience rapid motion. In this case, view-sharing techniques can be used for the remaining regions to further reduce the reconstruction time, as discussed below.

In the following paragraphs we will focus on a particular application: non-gated real-time imaging of cardiac function. We will describe a specific Kalman filter model and use this model to perform image reconstruction from undersampled data. Cardiac imaging has demanding requirements for a dynamic imaging method, because of the fast and complex motion of the heart combined with chest motion from breathing. First, we will introduce the implementation of the Kalman filter model and describe how to obtain the signal estimates. Then we will discuss several potential algorithms to simplify the model to reduce the reconstruction time. Finally we will discuss the combination of the Kalman filter with parallel imaging techniques.

5.2.1 Model Implementation

In a dynamic cardiac image series, the differences between two consecutive images are generally very small except for certain areas experiencing rapid changes; therefore, for simplicity, we can assume the state transition matrix is an identity matrix and the difference can be modeled as system noise having a zero-mean Gaussian distribution [20]. In fact, the variance of this system noise can represent the degree of variation at each corresponding pixel as the absolute value of the image differences are generally larger in more dynamic areas and smaller in less dynamic areas.

Therefore, together with the 1D simplification, the Kalman filter model for real-time cardiac function imaging can be written as

$$\begin{aligned} \mathbf{x}_k &= \mathbf{x}_{k-1} + \omega_{k-1}, \qquad \omega_k \sim N(\mathbf{0}, \mathbf{Q}_k) \\ \mathbf{z}_k &= \mathbf{F}_k \mathbf{x}_k + \nu_k, \qquad \nu_k \sim N(\mathbf{0}, \mathbf{R}_k) \end{aligned} \tag{5.3}$$

where $\mathbf{x}_k$ is simplified to be the image column vector assuming the row vector is along the readout direction for the 2D image, ω_k is the system noise vector with covariance matrix $\mathbf{Q}_k$, $\mathbf{F}_k$ is the 1D Fourier transform matrix, $\mathbf{z}_k$ is the corresponding k-space data column vector after the 1D Fourier transform along the readout direction, and ν_k is the measurement noise with covariance matrix $\mathbf{R}_k$. Given the initial estimate $\hat{\mathbf{x}}_0$ and the initial estimation error covariance matrix $\mathbf{P}_0$, the subsequent estimation of $\hat{\mathbf{x}}_k$ is given as

$$
\begin{aligned}
\hat{\mathbf{x}}_k^- &= \hat{\mathbf{x}}_{k-1}^+ \\
\hat{\mathbf{x}}_k^+ &= \hat{\mathbf{x}}_k^- + \mathbf{K}_k[\mathbf{z}_k - \mathbf{F}_k\hat{\mathbf{x}}_k^-] \\
\mathbf{P}_k^- &= \mathbf{P}_{k-1}^+ + \mathbf{Q}_{k-1} \\
\mathbf{K}_k &= \mathbf{P}_k^-\mathbf{F}_k^T[\mathbf{F}_k\mathbf{P}_k^-\mathbf{F}_k^T + \mathbf{R}_k]^{-1} \\
\mathbf{P}_k^+ &= [\mathbf{I} - \mathbf{K}_k\mathbf{F}_k]\mathbf{P}_k^-
\end{aligned}
\tag{5.4}
$$

where $\mathbf{P}_k$ is the estimation error covariance matrix at each time step k and is a vital intermediate parameter to calculate the Kalman gain matrix $\mathbf{K}_k$.

5.2.2 Parameter Estimation

From Eq. (5.4) we can see that the parameters that need to be estimated include the system noise covariance matrix $\mathbf{Q}_k$, the measurement noise covariance matrix $\mathbf{R}_k$, the initial state estimate $\hat{\mathbf{x}}_0$, and the initial estimation error covariance matrix $\mathbf{P}_0$.

First, we make an assumption that the distributions of the system noise vector ω_k and the measurement noise vector ν_k do not change during the scan, because the dynamic process (e.g., periodic cardiac motion) is stable from a statistical point of view. With this assumption, we have $\mathbf{Q}_k = \mathbf{Q}$ and $\mathbf{R}_k = \mathbf{R}$. The estimation of $\mathbf{Q}$ and $\mathbf{R}$ are discussed below.

In Sümbül's paper [20], as discussed before, $\mathbf{Q}$ was assumed to be a diagonal matrix to simplify the computation process. This assumption was also validated in the paper by determining that the cross-correlation terms of $\mathbf{Q}$ were very small, as shown in Fig. 1 of [20]. The diagonal $\mathbf{Q}$ was then roughly estimated from a low spatial resolution training scan covering only the center of k-space or more precisely estimated from multiple training scans covering different portions of k-space in each scan.

In our model, the diagonal assumption of $\mathbf{Q}$ is not necessary from a computational point of view due to the 1D simplification; therefore, in theory it is possible to use a general covariance matrix $\mathbf{Q}$ in which the off-diagonal term can reflect the relationships among neighboring pixels to provide a better estimation of the image column vector $\mathbf{x}_k$. However, in practice, it is difficult to estimate $\mathbf{Q}$, since no prior information about the distribution of ω_k is given and thus we must rely solely on the sample observations of ω_k. From statistics, for an N-dimensional vector ω_k, the number of observations should be much greater than N to provide a reliable estimate of its covariance matrix $\mathbf{Q}$. For MRI, N is usually very large and hence the amount of training data needed would be even larger, which would result in an extremely long training scan. Furthermore, the error in the estimation of a general covariance matrix $\mathbf{Q}$ can sometimes cause divergence of the Kalman filter model. On the other hand, if we assume $\mathbf{Q}$ is a diagonal matrix and ignore the cross-correlation terms, the estimation of $\mathbf{Q}$ becomes a pixel-by-pixel problem; only the variance of ω_k at each pixel needs to be estimated and the required sample observations can be greatly reduced. As compared with a potentially inaccurate general covariance matrix $\mathbf{Q}$, a diagonal but more accurate $\mathbf{Q}$ is used in our model, and the accuracy of this simplification will be demonstrated in the simulation study described below.

To estimate the diagonal terms of $\mathbf{Q}$, we use a low-resolution training scan that only acquires the center k-space lines. The fraction of the k-space lines acquired for the training is determined by the undersampling ratio in data acquisition so that the temporal resolution of the training images is the same as that of the actual images. Although the accuracy of the variance estimation can be impaired at sharp edges in the image with a low-resolution training scan due to blurring, we have found the error in pixel variance estimation to be acceptable, because the Kalman filter uses all previous measurements to arrive at the current estimate and thus exploits the overall redundancy of the k-space data.

An alternative way to estimate $\mathbf{Q}$ is to use multiple training scans to cover different parts of k-space, similar to the use of different spiral rings as introduced in [20]. However, this requires multiple training scans and thus greatly increases the scan time. Furthermore, the effect of this more precise $\mathbf{Q}$ is not obvious in terms of the accuracy of the state vector estimate, which is our ultimate goal. Therefore, we prefer to use the low-resolution training scan to get $\mathbf{Q}$. The accuracy of this approach will also be demonstrated in the simulation study described below.

In our estimation process, we use the differences between magnitude images rather than complex images to estimate the variance at each pixel. When using complex differences, differences in phase that result from off-resonance, motion or noise between consecutive training images can significantly increase the variance and thus make the estimate unreliable. This is especially true in regions where the image magnitude is small. The measurement noise can also affect the estimation of $\mathbf{Q}$, but this can be corrected as described in the following paragraph.

To estimate $\mathbf{R}_k$, we also use the diagonal and time-invariant assumptions, since the measurement noise can be regarded as independent white noise and does not change with time. Therefore, we have $\mathbf{R}_k = \mathbf{R} = \sigma^2\mathbf{I}$, where $\mathbf{I}$ is the identity matrix. It is necessary to mention that this noise is not the original

2D k-space measurement noise but the noise after a 1D Fourier transform along the readout direction; however, since the Fourier transform is an orthonormal transform, the whiteness of the noise is maintained. As discussed before, the estimation of $\mathbf{Q}$ is contaminated with measurement noise because the training data measurement is not noise-free and the noise is brought into the training images via the Fourier transform. Assuming the raw estimation of $\mathbf{Q}$ is given as $\mathbf{Q}_{raw}$, we can derive that $\mathbf{Q} = \mathbf{Q}_{raw} - 2c\sigma^2\mathbf{I}$, where c is a constant determined by the normalization factor of the Fourier transform. To jointly correct for the contamination of measurement noise to get $\mathbf{Q}$ and estimate the noise level σ, we simply make the assumption that the minimum diagonal term of $\mathbf{Q}$ is close to zero, because there exists at least one pixel that stays almost the same during the dynamic process and consequently, the minimum diagonal term in $\mathbf{Q}_{raw}$ is due to the measurement noise. So we can get the estimate of σ and the corrected $\mathbf{Q}$.

Finally, we need to initialize the model with the initial conditions of $\hat{\mathbf{x}}_0$ and its estimation error covariance matrix $\mathbf{P}_0$. It is impossible to provide an accurate and alias-free initial image due to limited temporal and spatial resolution. The options are either the spatially-blurred image from the low-resolution training scan or the temporally-blurred image reconstructed using view sharing techniques. However, since the Kalman filter is a robust filter that can correct for the inaccuracy in the initial estimates with more and more measurements, the influence of the inaccuracy of the initial image will fade away; therefore, we choose an initial image with faster convergence. The performance of these two options are compared with the simulation study described in the following sections. Similarly, the inaccuracy in $\mathbf{P}_0$ will also be corrected by the Kalman filter; therefore, we just empirically choose it to be $\mathbf{Q}$ multiplied by the undersampling ratio, because the estimation error of $\hat{\mathbf{x}}_0$ at one pixel is roughly proportional to the variance of that pixel and the undersampling ratio.

5.2.3 Simplifications of the Kalman Filter Model

From Eq. (5.4) we can see that the most time-consuming step is the calculation of the Kalman gain matrix $\mathbf{K}_k$ and the intermediate parameter $\mathbf{P}_k$. However, as discussed before, the system noise covariance matrix $\mathbf{Q}$ and the measurement noise covariance matrix $\mathbf{R}$ are assumed to be time-invariant; therefore, the only matrix that changes from step to step involved in calculation of $\mathbf{K}_k$ and $\mathbf{P}_k$ is the measurement matrix $\mathbf{F}_k$. If the k-space sampling pattern is periodic over the entire image series, the corresponding matrix $\mathbf{K}_k$ is also periodic. Because $\mathbf{P}_0$ is a manually chosen parameter, the Kalman gain matrix $\mathbf{K}_k$, as well as $\mathbf{P}_k$, will gradually converge to a periodic steady state after several steps. After that, the update of $\mathbf{K}_k$ using Eq. (5.4) can be replaced by using the pre-calculated periodic $\mathbf{K}_k$. The reconstruction time can thus be greatly reduced. The convergence of $\mathbf{K}_k$ is demonstrated with the simulation study in the following sections.

In addition, as discussed before, we do not have to use the Kalman filter model for every phase encoding line. Each phase encoding line corresponds to one readout location after the 1D Fourier transform along the readout direction. If this phase encoding line is within a static or slowly-varying area, simple view sharing methods are sufficient to reconstruct this line without aliasing, and thus the reconstruction time can be reduced. Instead of retrospectively selecting these areas, $\mathbf{Q}$ can provide this information, because in static or slowly varying areas the corresponding variance is very small compared to that in more dynamic areas. Specifically, we examine the variance vector $\mathbf{Q}_l$ that corresponds to each readout location and determine whether $max(\mathbf{Q}_l) < \mathbf{Q}_{mean}/2$, where $\mathbf{Q}_{mean}$ is the mean variance across the entire 2D image. If this is true, then we use a linearly interpolated view sharing method (SLAM) instead of the Kalman filter model. The effect of this simplification is examined in the simulation study below.

5.2.4 Kalman Smoother

If a strict real-time reconstruction is not required, the Kalman smoother can be used to improve the estimation result of the Kalman filter. In fact, the fixed-lag Kalman smoother, which estimates the current state $\mathbf{x}_k$ with all measurements before $\mathbf{z}_{k+\Delta}$, can realize an approximate real-time reconstruction as long as the fixed lag Δ is not very large. The detailed calculation of the Kalman smoother estimate $\mathbf{x}_{k|k+\Delta}$ based on the Kalman filter estimate $\mathbf{x}_k$ and the estimation error covariance matrix $\mathbf{P}_k$ is given in [69] and is omitted here for simplicity.

In practice, the lag is chosen to be the undersampling ratio so that an additional fully sampled k-space data set is acquired before the estimation of the current frame. The effect of the Kalman smoother is examined in the simulation study below.

5.2.5 Multiple Coils

If multiple receiver coils are used, we can extend the Kalman filter model to incorporate the measurements from different coils by combining the Kalman filter with SENSE. If the coil sensitivity map is available, we can include the data from different coils, which results in the following model [20]

$$\begin{aligned} &\mathbf{x}_k = \mathbf{x}_{k-1} + \omega_{k-1}, && \omega_k \sim N(\mathbf{0}, \mathbf{Q}_k) \\ &\begin{bmatrix} \mathbf{z}_{k1} \\ \mathbf{z}_{k2} \\ \vdots \\ \mathbf{z}_{kn} \end{bmatrix} = \begin{bmatrix} \mathbf{F}_k\mathbf{S}_{k1} \\ \mathbf{F}_k\mathbf{S}_{k2} \\ \vdots \\ \mathbf{F}_k\mathbf{S}_{kn} \end{bmatrix} \mathbf{x}_k + \begin{bmatrix} \nu_{k1} \\ \nu_{k2} \\ \vdots \\ \nu_{kn} \end{bmatrix}, && \nu_{ki} \sim N(\mathbf{0}, \mathbf{R}_{ki}) \end{aligned} \tag{5.5}$$

where n is the number of receiver coils and $\mathbf{S}_{kn}$ is the coil sensitivity map. For generality, the coil sensitivity map is assumed to be time-variant, because in imaging during free breathing, the chest motion can cause the coil elements to move. To dynamically estimate the coil sensitivity map, we use the coil images reconstructed with view sharing techniques. Correct normalization of the coil sensitivity map is important to avoid divergence of the Kalman filter solution. The disadvantages of using this SENSE-based method include difficulty in accurately estimating the coil sensitivity map in dynamic imaging and greatly increased computation. The computation increases because the dimension of the measurement model is increased by n and the periodic property of the Kalman gain matrix $\mathbf{K}_k$ is lost, because the measurement matrix is no longer periodic due to non-periodic $\mathbf{S}_{kn}$. Therefore, we also developed a method of combining the Kalman filter with GRAPPA to more effectively use the multi-coil measurements.

Compared with traditional GRAPPA, TGRAPPA is advantageous in dynamic cardiac imaging since no separate training step is required and the GRAPPA kernel is updated for every frame in the image series [66]. In our model, first we use the updated GRAPPA kernel to fill all the missing k-space lines for each individual coil. We know that the filled k-space data is not accurate enough to generate an alias-free and high SNR image when the undersampling ratio is very high if we just do a Fourier transform and combine the coil images, as in TGRAPPA. However, we can still input this approximate k-space data into the modified Kalman filter model as follows

$$\begin{aligned} &\mathbf{x}_k = \mathbf{x}_{k-1} + \omega_{k-1}, && \omega_k \sim N(\mathbf{0}, \mathbf{Q}_k) \\ &\begin{bmatrix} \mathbf{z}_k \\ \mathbf{z}_{k\_TG} \end{bmatrix} = \mathbf{F}\mathbf{x}_k + \begin{bmatrix} \nu_k \\ \nu_{k\_TG} \end{bmatrix}, && \begin{bmatrix} \nu_k \\ \nu_{k\_TG} \end{bmatrix} \sim N(\mathbf{0}, \begin{bmatrix} \mathbf{R}_k & \mathbf{0} \\ \mathbf{0} & \mathbf{R}_{k\_TG} \end{bmatrix}) \end{aligned} \tag{5.6}$$

where $\mathbf{z}_k$ is the measured k-space data and $\mathbf{z}_{k\_TG}$ is the unacquired k-space data estimated from $\mathbf{z}_k$ and the corresponding GRAPPA kernel; $\mathbf{F}$, which replaces $\mathbf{F}_k$ in the original model, is now the fully sampled 1D Fourier transform matrix, since $\mathbf{z}_k$ and $\mathbf{z}_{k\_TG}$ together cover all of k-space. It is worth mentioning that the measurement noise covariance matrix $\mathbf{R}_{k\_TG}$ corresponding to $\mathbf{z}_{k\_TG}$ is no longer determined by the actual k-space measurement noise, since $\mathbf{z}_{k\_TG}$ is not the measured k-space data. On the contrary, $\mathbf{R}_{k\_TG}$ reflects the reliability of the filled k-space data using the GRAPPA kernel by considering the deviation of the filled k-space data from the "true" k-space data as noise. Similarly with $\mathbf{R}_k$, for simplicity, $\mathbf{R}_{k\_TG}$ is also assumed as white and time-invariant, given as $\mathbf{R}_{k\_TG} = \mathbf{R}_{TG} = p^2\sigma^2\mathbf{I}$, in which p describes the reliability of the filled data relative to the measurement noise. In fact, the off-diagonal terms of $\mathbf{R}_{k\_TG}$ are not exactly zero as the missing k-space data points in one frame are generated using the same TGRAPPA kernel; the results might be more accurate with an approximate model to handle the noise related to TGRAPPA, but this is beyond the scope of this dissertation. Empirically, we have observed that $p = 6r^2/n$, in which r is the undersampling ratio and n is the number of the coils. It is assumed that with a larger undersampling ratio, the standard deviation of the filled k-space data increases much faster and can be modeled with a square relationship. By this modified model, we can efficiently combine the spatial parallel information with the temporal model to give a better estimate of the dynamic image series. Also, with each coil, from Eq. (5.4), the Kalman gain matrix $\mathbf{K}_k$ can still converge to save reconstruction time, since $\mathbf{Q}_k$, $\mathbf{R}_k$ and $\mathbf{R}_{k\_TG}$ are time-invariant and $\mathbf{F}$ is a constant.

5.3 Methods

5.3.1 Simulations

To verify the basic concept of the Kalman filter model in dynamic MRI, we first did a numerical phantom study by constructing a dynamic image series containing three pairs of concentric circles with fixed radius, slowly oscillating radius and rapidly oscillating radius, respectively. To simulate the data acquisition process using a Cartesian trajectory, we calculated the instant image at a given time point and its Fourier transform and selected the corresponding k-space data of one phase encoding line assuming the actual measurement was done at that time point. The training data used for the Kalman filter model was simulated using the same method before the data acquisition. Then we reconstructed the simulated data set using sliding window, SLAM and the Kalman filter model with an acceleration factor of 2.

To study the effect of the Kalman filter model in reconstruction of undersampled data, we then conducted a series of more realistic simulations, where we reconstructed the image series after retrospectively throwing out a portion of the k-space data and then compared the reconstructed image series with the fully sampled data. The baseline image series were acquired using a balanced SSFP sequence in a real-time ungated cardiac MRI (CMR) study under both breath-hold and free-breathing situations. 2x TGRAPPA was used to increase the temporal resolution. A total of 80 frames covering approximately 9 heart cycles were generated. Then we did a Fourier transform for the baseline image series to get the fully sampled k-space data and manually undersampled that using a given sampling pattern with undersampling ratio 2 and/or 4. The training data for parameter estimation was also obtained from the fully-sampled k-space data of the first 40 frames by selecting the center 1/2 or 1/4 of the k-space data.

To study the effect of $\mathbf{Q}$ in the Kalman filter model, in addition to the diagonalized $\mathbf{Q}$ estimated from the low-resolution training data, we also obtained a diagonalized $\mathbf{Q}$ and a non-diagonalized $\mathbf{Q}$ with fully-sampled training data in which no manual undersampling was performed. The performance of the Kalman filter model using these three $\mathbf{Q}$s were compared by calculating the root mean square differences between the reconstructed image series and the baseline image series. Similarly, to study the effect of the initial image in the Kalman filter model, we used the spatially-blurred initial image and the temporally-blurred initial image and compared the root mean square differences.

In addition, to test the simplifications of the Kalman filter model, we implemented the original Kalman filter model without any simplifications, the Kalman filter model with the convergent simplification and the Kalman filter model with the convergent simplification and combined with SLAM. We compared their performances based on the root mean square differences.

For these simulations, a periodic sampling pattern is required when evaluating the convergence of the Kalman filter. Therefore, we used four types of sampling patterns satisfying the periodic requirement and compared their performance. For types I-III, we first fixed the phase encoding line order for a fully-sampled data set and then selected a subset of phase encodings corresponding to one frame based on the undersampling factor. The subsets selected for Type I were interleaved, those for type II were bit-reversed, and those for type III were random. For type IV, we generated a collection of random k-space lines based on the undersampling factor and repeated this collection for every frame.

Finally, to compare the Kalman filter method and the fixed-lag Kalman smoother method with other available real-time reconstruction methods represented by view sharing techniques, we also implemented the sliding window method and SLAM. Furthermore, we used kt-FOCUSS as a representative of iterative reconstruction methods based on compressed sensing and compared it with the Kalman filter method with the same undersampling factor but a Gaussian random undersampling pattern. In addition to the root mean square differences between the reconstructed image series and the baseline image series, we also calculated the structural similarity index, which measures the similarity between two images based on human eye perception to better estimate the performance of each reconstruction method.

5.3.2 Experiments

Ungated real-time cardiac imaging experiments were performed on a Siemens Avanto 1.5 T scanner (Erlangen, Germany) equipped with a 12-channel body coil array and a 32-channel body coil array. We used both coils in our experiments. A 2D Cartesian bSSFP sequence was used with sequence parameters as follows: TR = 2.14 ms, TE = 1.07 ms, FOV = 380∼400 mm, slice thickness = 8 mm, flip angle = 46 °, number of PE lines = 128, number of RO samples = 128, image matrix size = $128 * 128$. A training scan of about 2.5 s was performed before the data acquisition to collect the center k-space lines. The total scan time was about 10 s. Both short axis and long axis views of the heart were imaged under breath held and free breathing conditions with acceleration factor 4. Array compression [70] was used for the primary coil data to simplify the calculation process for the large coil arrays. The data was then reconstructed using sliding window, SLAM, TGRAPPA, KF-SENSE and KF-TGRAPPA.

In order to independently assess the extent of spatial aliasing and to assess the image quality of rapid moving structures, two cardiologists (M.S. and C.M.K) graded the images for the severity of spatial aliasing and temporal blurring each on a 5-point scale. The ratings were then statistically analyzed with a two-tailed Wilcoxon test. For the spatial aliasing assessment a score of 1 corresponded to very severe aliasing precluding evaluation of myocardial function; 2 to severe aliasing but adequate to evaluate function; 3 to mild-moderate aliasing but not affecting region of interest; 4 to mild aliasing; and 5 to no aliasing. The perceived temporal blurring was graded as a score of 1 for virtually no temporal information; 2 for severe temporal blurring limiting ability to assess function; 3 for temporal blurring evident, but not affecting assessment of LV function; 4 for mild temporal blurring evident; and 5 for no temporal blurring. The image reviewers are both level III trained in CMR and have 6 and 20 years experience interpreting clinical CMR images.

5.4 Results

5.4.1 Simulations

Figure 5.1 gives the results for the numerical phantom simulation in which the reconstructed images at one time point (top row) and the image intensities along one vertical line versus time (bottom row) using sliding window, SLAM and the Kalman filter model are shown. The three pairs of concentric circles, from left to right, are with fixed radius, slowly oscillating radius and rapidly oscillating radius, and the red lines indicate the image cross-section displayed in the bottom row. The ghost artifacts due to the change in radius are very obvious with the sliding window and SLAM methods, but are greatly reduced with the Kalman filter model. In addition, the temporal resolution with the Kalman filter is much higher than with the two view sharing methods, as can be seen in the images in the bottom row. Temporal blurring can be seen both by the smoothing of the peaks as a function of time and by spatial blurring vertically between the white center region (simulated left ventricle) and the gray outer region (simulated myocardium). This improved temporal resolution comes from the fact that the Kalman filter model can distinguish the more dynamic areas from the less dynamic areas and hence more effectively use the undersampled data to catch

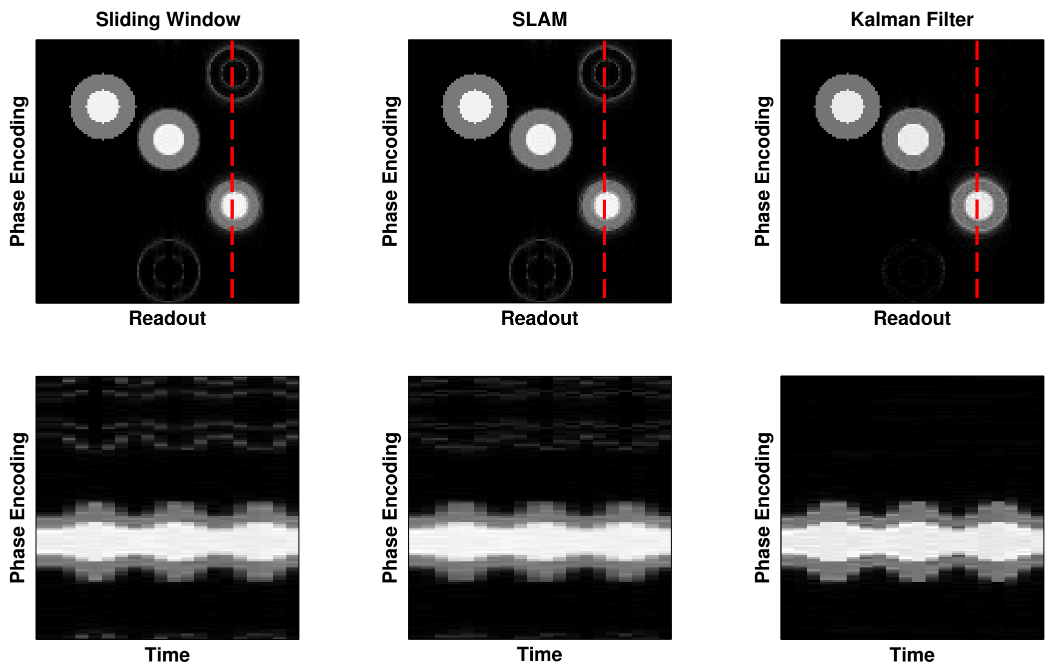

Figure 5.1: *Numerical phantom simulation with SW, SLAM and the Kalman filter method.*

the movement in the more dynamic areas.

Figure 5.2 plots the root mean square differences between the reconstructed image series and the baseline image series using a diagonalized $\mathbf{Q}$ estimated from the low-resolution training data and from the fully-sampled training data (left) and using the spatially-blurred initial image and the temporally-blurred initial image (right). The reconstructed image series using a general $\mathbf{Q}$ estimated from the fully-sampled training data diverges, indicating the Kalman filter model fails with such an inaccurately estimated $\mathbf{Q}$. The left side of Fig. 5.2 indicates that the result using the low-resolution training data is very similar to the fully-sampled training data or even performs better (lower root mean square differences) for

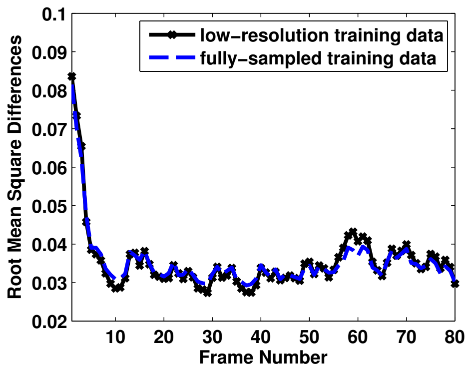

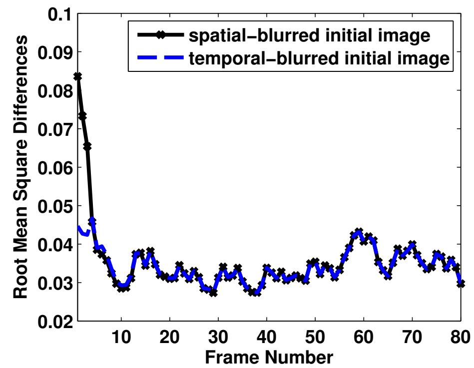

Figure 5.2: *Root mean square differences of the Kalman filter model using different* $\mathbf{Q}$ *(left) and initial images (right).*

certain frames. Therefore, this data indicates that it is unnecessary to use multiple scans for a more precise $\mathbf{Q}$. The right side of Fig. 5.2 shows that the choice of initial image is not critical, because both initial images give the same results after approximately 10 frames. However, even though the root mean square differences are larger with the spatially blurred initial image in the beginning, they converge faster as the values drop faster than with the temporally blurred initial image. Therefore, we chose the spatially blurred initial image in our experiments.

The left side of Fig. 5.3 shows the root mean square differences of the reconstructed image series and the baseline image series using the original Kalman filter model, the convergent Kalman filter model and the convergent Kalman filter model combined with SLAM. It indicates that the results using the original algorithm and the two simplified algorithms are almost identical, meaning the simplifications of the Kalman filter model do not harm the effectiveness of the model. The right side of Fig. 5.3 plots the value of $\mathbf{K}_k$ at a fixed location with the original Kalman filter model. The result conforms to our expectation as $\mathbf{K}_k$

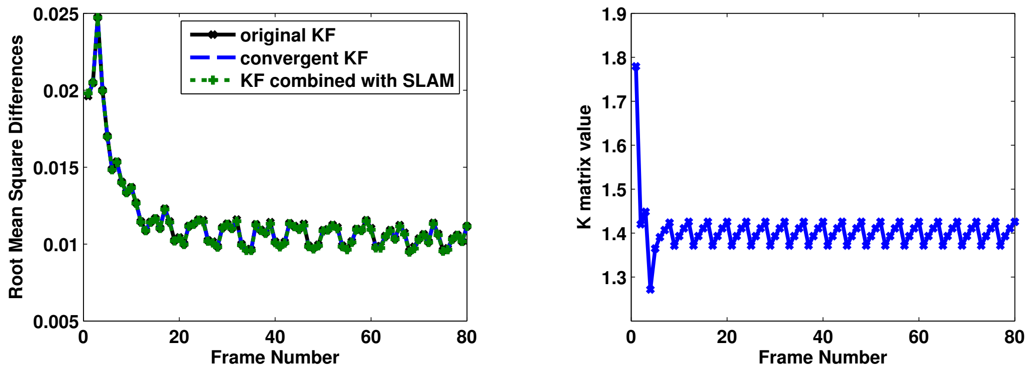

Figure 5.3: *Left: Root mean square differences of the Kalman filter model using the original algorithm and the simplified algorithms. Right: Simulation demonstrating that* $\mathbf{K}_k$ *approaches a periodic steady state.*

approaches a periodic steady state with period 4, which is the undersampling ratio used in this simulation. Therefore, in practice we use the convergent Kalman filter model combined with SLAM to maximally reduce the reconstruction time.

Figure 5.4 plots the 4 types of sampling patterns (left) and the resulting root mean square differences using these sampling patterns. There are no apparent differences among the first three types of the sampling patterns in terms of root mean square differences and they all perform better than the fourth type of the sampling pattern. This shows that a sampling pattern that covers the entire k-space in several frames is preferred. This is because the Kalman filter relies on all previous measurements to give an optimal estimate of the current state, so acquiring all of k-space provides comprehensive information to better estimate the current image, even though the k-space acquisition is completed over several frames.

Figure 5.5 shows example images reconstructed using the sliding window, SLAM, kt-FOCUSS, Kalman filter and Kalman smoother with undersampling ra-

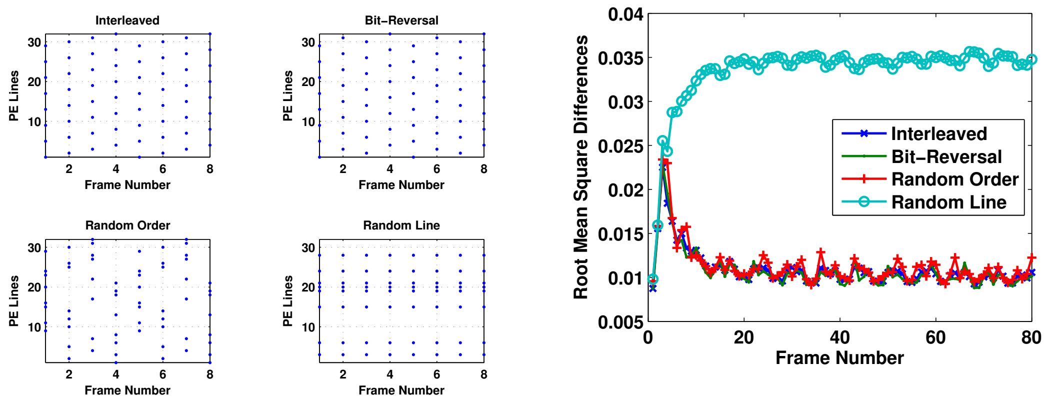

Figure 5.4: *Root mean square differences of the Kalman filter model using different sampling patterns.*

tio of 2 (top row), the corresponding difference images with the raw image (middle row) and the image intensities of one phase encoding line as indicated in the top left image across the entire image series (bottom row) in a single-coil simulation study with a free breathing short axis image series. The ghost artifacts due to motion are obvious in the sliding window and SLAM methods and are greatly alleviated with Kalman filter and smoother methods. The aliasing pattern with kt-FOCUSS is different from the other methods due to the non-linearity of the reconstruction. In addition, some blurring occurs in free-breathing situations as illustrated by the arrows in Fig. 5.5. The images along the bottom row show that the Kalman filter and the Kalman smoother provide the highest temporal resolution as the changes of the left ventricle radius are the sharpest. Figure 5.6 shows a plot of the root mean square error (RMSE) and the structural similarity index (SSIM) between the reconstructed image series and the raw image series in the same simulation study. The Kalman filter and smoother provide a lower RMSE and a higher SSIM compared with sliding window (SW) and SLAM in most of our simulation studies with undersampling ratios of 2 and 4, including the study shown in Fig. 5.5. As shown in Fig. 5.6, the decrease of RMSE and increase of SSIM are more obvious in frames when the cardiac motion is very fast, such as the end-systolic phase of the cardiac cycle. Comparing the Kalman filter with kt-FOCUSS, kt-FOCUSS yielded the lowest RMSE in most breath-held simulations; however, with free-breathing simulations, kt-FOCUSS sometimes had higher RMSE than the Kalman filter method. The Kalman smoother can further reduce the RMSE and increase the SSIM compared with the Kalman filter since more information is incorporated for the estimation with a minor sacrifice of increased latency.

5.4.2 Experiments

Figure 5.7 shows the results of the blind review for a total of 8 experiments including 4 short axis and 4 long axis experiments with acceleration factor 4. The visually assessed temporal resolution is improved with TGRAPPA, KF-SENSE and KF-TGRAPPA (KF-TG) compared with sliding window and SLAM and the improvement was statistically significant from the two-tailed Wilcoxon signed rank test ($p < 0.05$ for SW vs. KF-SENSE, SW vs. KF-TG, SLAM vs. KF-SENSE, SLAM vs. KF-TG). For the degree of spatial aliasing, the ratings of KF-SENSE and KF-TGRAPPA were not statistically different from sliding window and SLAM, although KF-SENSE and SLAM were slightly better than SW and KF-TG. Comparing KF-TGRAPPA with TGRAPPA, there was significant reduction in spatial aliasing ($p < 0.05$) and slightly better temporal resolution.

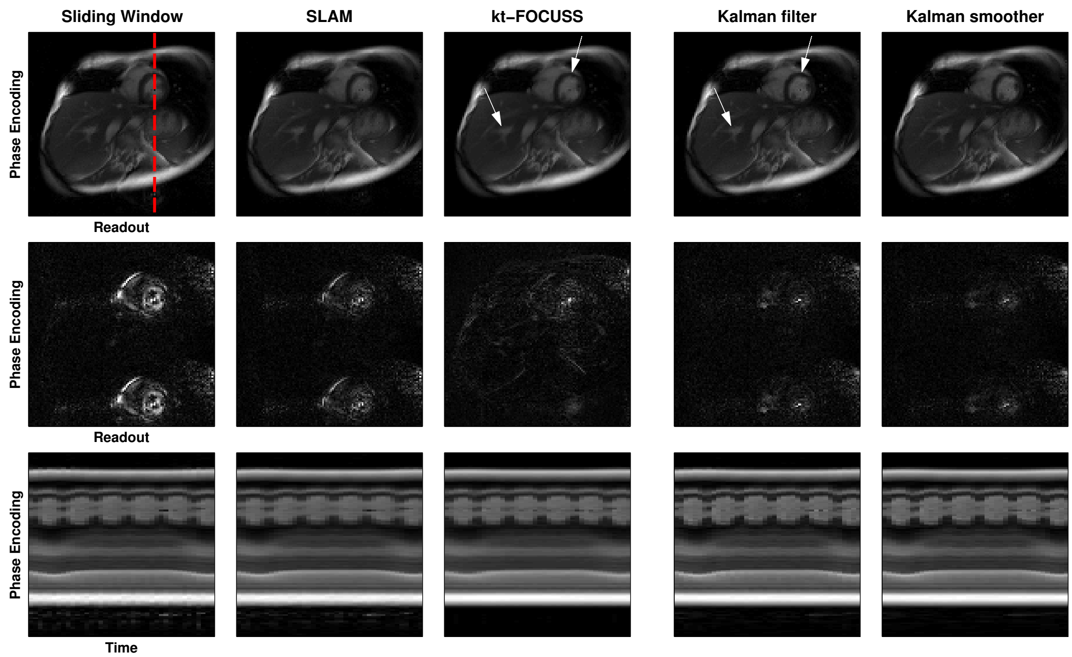

Figure 5.5: *Images reconstructed using sliding window, SLAM, kt-FOCUSS, Kalman filter and Kalman smoother methods with undersampling factor of 2 (top row), the corresponding difference images with the raw image (middle row) and the image intensities along the red vertical line (top left image) as a function of time (bottom row).*

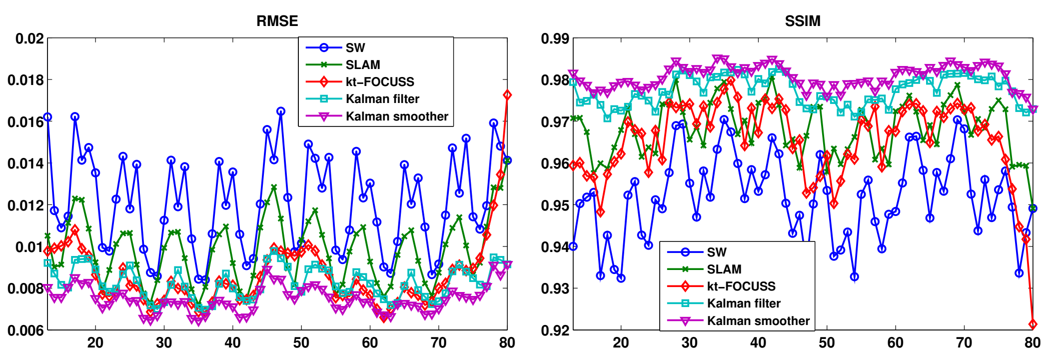

Figure 5.6: *RMSE(left) and SSIM(right) between the reconstructed image series and the raw image series.*

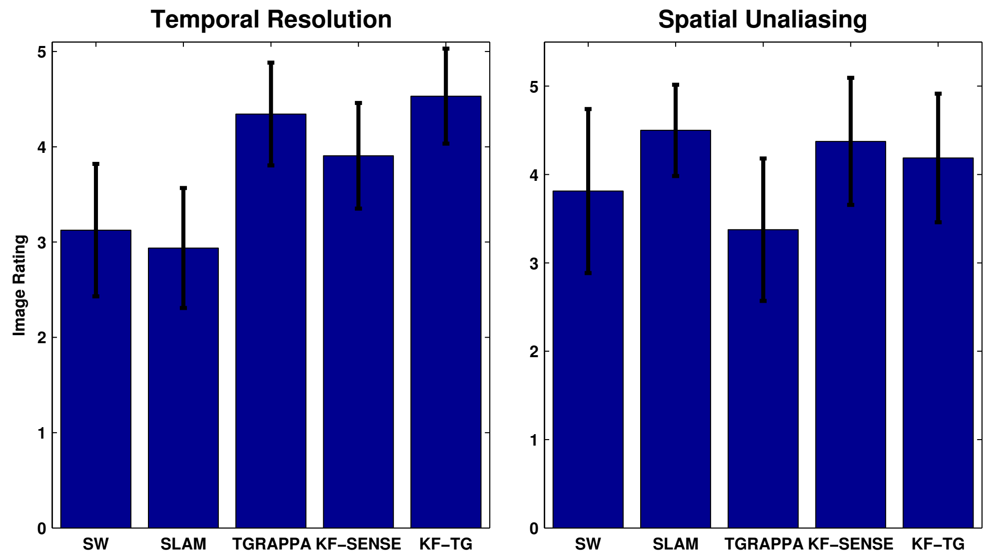

Figure 5.7: *Temporal resolution and spatial unaliasing ratings by two blinded expert readers.*

5.5 DISCUSSION

We have developed a Kalman-filter-based image reconstruction method for real-time reconstruction of Cartesian dynamic image series and implemented it in a real-time CMR study. We combined the model with SENSE and TGRAPPA. The major advantages of this method include the capability for non-iterative real-time reconstruction and significantly improved temporal resolution. The capability for non-iterative real-time reconstruction lies in the fact that as long as the model is established, the Kalman filter can generate an optimal estimate of the current state given all previous measurements with a single prediction-correction process without iteration. The reconstruction in this study was performed offline using Matlab and has not yet been implemented on the scanner's reconstruction computer. However, the computational load is relatively small and can be realized with moderate computing hardware. The offline reconstruction time for an entire image series (80 frames, $128 * 128$) is about 4 seconds in Matlab using a laptop with a 2.2 Ghz CPU and without parallel computing. This corresponds to a computation time of 50 ms per temporal frame. Furthermore, as discussed previously, if the sampling pattern is periodic, the major computation, which is the calculation of the Kalman gain matrix $\mathbf{K}_k$, can be performed before the data acquisition and thus the subsequent reconstruction requires only two matrix-vector multiplications and one vector-vector addition per readout pixel. In addition, the algorithm is easily parallelizable, because each readout pixel can be treated independently; thus, parallel computing can be easily implemented to reduce the reconstruction time.

The improvement in temporal resolution with this method is because the Kalman filter can capture rapid changes with limited measurements. For example, if the k-space measurements are under-sampled, the information is not enough to get an accurate current estimate from just that data; however, the relationship between the current and the past states represented by the state model can be exploited to benefit the current estimate. In this study, the pixels with lower variance rely more on past states by the prediction step; the pixels with larger variance rely more on the measurements by the correction step. Therefore, since the number of pixels with large variance is much smaller than the total number of pixels, the information contained in the k-space measurements is sufficient to provide an accurate current estimate.

A fixed-lag Kalman smoother was also realized with a relatively short lag to improve the estimation when strict real-time reconstruction is unnecessary.

Although in this dissertation we focused on a real-time cardiac study, the model is not limited to this application. In this application, we make a simple assumption to just copy the previous state to get the current state. For other applications, the model might need some modifications if we can get some information about the evolution of the states. However, the framework of simplifying the 2D problem to a 1D problem makes it easier to modify and implement a more complicated model such as an autoregressive-moving-average (ARMA) model to more accurately describe the relationships among the states.

The combination of the Kalman filter with parallel imaging techniques can further reduce scan time and improve image quality, as demonstrated by KF-SENSE and KF-TGRAPPA. Both are suitable for real-time reconstruction, although KF-SENSE is more computationally demanding, resulting in longer image reconstruction times. The coil sensitivity estimation in KF-SENSE can be further explored to improve image quality. For KF-TGRAPPA, the error covariance of the filled k-space data in this chapter is not an optimal choice but simply an empirical one. Therefore, further research is necessary to reduce the spatial aliasing by tuning this parameter.

Upon visual analysis, the improvement in temporal resolution is obvious with the Kalman filter; however, the cardiologists who scored the images were not bothered by some aliasing artifacts that were apparent in difference images in the simulation study, because they mainly focused on the cardiac region and the aliasing was relatively small in that region. There are some flickering artifacts with the Kalman filter model that lead to a lower rating in spatial unalising. Further study is needed to provide a more comprehensive understanding of the advantages and disadvantages of the Kalman filter model.

The combination of the fixed-lag Kalman smoother with TGRAPPA was also realized and provides improved spatial unaliasing. However, the rating was performed before this development and thus does not include this KS(Kalman smoother)-TGRAPPA. Further validation is required to evaluate this improvement.

In conclusion, the Kalman filter method is a novel real-time reconstruction method in dynamic MRI that can improve temporal resolution. The potential for real-time reconstruction may be valuable compared with retrospective and/or iterative reconstruction methods. The versatility of the model is also an advantage and is a promising topic for future study.

Chapter 6

Conclusion

Dynamic MRI is becoming a more and more active research area as researchers seek to expand the application of MRI in medicine. Various techniques have been developed to reduce scan time and many new applications have been explored to take advantage of these techniques. In this dissertation, we aimed to explore dynamic MRI techniques and applications in three different projects. Before delving into them, we discussed several general techniques in spiral scanning, since it is a very fast k-space sampling method but the image quality can be impaired by off-resonance effects, trajectory infidelity and DCF calculation.

The first project we explored was the comparison of radial, spiral-out and spiral-in/out bSSFP sequences in real-time cardiac function MRI. We implemented a spiral-out bSSFP sequence and developed a new spiral-in/out bSSFP sequence to explore the refocusing mechanism and its potential utilization for fat-water separation. The comparison results demonstrated that both spiral bSSFP sequences are advantageous compared with a radial bSSFP sequence in this application, mainly due to the different acceleration scheme of the radial and spiral trajectory. The refocusing mechanism of spiral-in/out bSSFP sequence can provide enhanced SNR and reliable fat-water separation.

The second project we explored includes spiral parallel imaging techniques and their application in real-time velum imaging. To further reduce the scan time, spiral scanning can be combined with spatial and temporal parallel imaging techniques by exploiting the redundancy in the k-space data from multiple receiver coils and the temporal correlation of dynamic image series. We also explored a new dynamic MRI application – real-time velum imaging – by developing a dynamic spiral sequence and experimenting the appropriate protocol. Spiral parallel imaging techniques were applied in this application to satisfy the demanding requirements for spatial and temporal resolution and SNR. The primary result of the dynamic velum image series showed the potential for using MRI as a new VPI diagnostic tool and to help velum muscle modeling.

The third project we explored involved Cartesian Kalman filter techniques and their application to real-time cardiac function MRI. These techniques provide a real-time imaging and reconstruction framework for reducing scan time with a Cartesian trajectory. The Kalman filter model describes the temporal relationships of a dynamic application, which can be used to estimate the current frame with undersampled k-space data. The combination with both SENSE and GRAPPA was also explored for a higher reduction factor. The application to real-time cardiac function MRI has been proved to reduce temporal blurring compared with view sharing methods and reduce spatial aliasing compared with spatial parallel imaging techniques.

6.1 Collaborations and Contributions

This dissertation includes many efforts from different collaborators inside and outside Dr. Craig Meyer's lab and it would not have been possible to finish it without all their work and help. The author will make the best effort to include all relevant collaborators but will apologize for those missed.

The general spiral reconstruction techniques are especially the result of teamwork in Dr. Craig Meyer's lab. The fast conjugate phase method based on a Chebyshev approximation was originally developed by Dr. Weitian Chen and Dr. Christopher Sica. The k-space trajectory estimation method was originally developed by Dr. Hao Tan and was further investigated by the author and Samuel Fielden for variations of the model and applications in other sequences. The cut-off Voronoi DCF was originally developed by the author but a similar idea had been investigated by Dr. Michael Salerno.

The three projects were mainly the work of the author. However, the real-time velum imaging using MRI was the idea of Dr. Silvia Blemker. Finally, needless to say, all the work in this dissertation is attributed to the guidance of Dr. Craig Meyer.

Bibliography

[1] CB Ahn, JH Kim, and ZH Cho, "High-speed spiral-scan echo planar NMR imaging-I.", *IEEE TRANS. MED. IMAG.*, vol. 5, no. 1, pp. 2-7, 1986

[2] CH Meyer, BS Hu, DG Nishimura, and A Macovski, "Fast spiral coronary artery imaging", *Magn Reson Med*, vol. 28, no. 2, pp. 203-213, 1992

[3] B Aldefeld, and P Bornert, "Effects of gradient anisotrophy in MRI", *Magn Reson Med*, vol. 39, no. 4, pp. 606-614, 1998

[4] J Mo, V Callot, T-Y Huang, BP Poncelet, and TG Reese, "A rapid and accurate automated in-vivo shimming application integrated with the Siemens 1.5T and 3T consoles", in *Proc. 12th Ann. Meeting of ISMRM*, Kyoto, Japan, p. 538, 2004

[5] JJ Van Valls, and AH Bergman, "Optimization of eddy-current compensation", *J Magn Reson*, vol. 90, pp. 52-70, 1990

[6] G Wider, V Doetsch, and K Wuethrich, "Self-compensating pulsed magnetic-field gradients for short recovery times", *J Magn Reson A*, vol. 108, pp. 255-258, 1994

[7] RD Hoge, RK Kwan, and GB Pike, "Density compensation functions for spiral MRI", *Magn Reson Med*, vol. 38, no. 1, pp. 117-128, 1997

[8] V Rasche, R Proksa, R Sinkus, P Bornert, and H Eggers, "Resampling of data between arbitrary grids using convolution interpolation", *IEEE Trans Med Imaging*, vol. 18, no. 5, pp. 385-392, 1999

[9] JG Pipe, and P Menon, "Sampling density compensation in MRI: rationale and an iterative numerical solution", *Magn Reson Med*, vol. 41, no. 1, pp. 179-186, 1999

[10] M Salerno, CM Kramer, and CH Meyer, "Myocardial Perfusion Imaging with Variable Density Spiral Trajectories", in *Proc. 18th Ann. Meeting of ISMRM*, Stockholm, Sweden, p. 3624, 2010

[11] AB Kerr, JM Pauly, BS Hu, KC Li, CJ Hardy, CH Meyer, A Macovski, and DG Nishimura, "Real-time interactive MRI on a conventional scanner", *Magn Reson Med*, vol. 38, no. 3, pp. 355-367, 1997

[12] S Kaji, PC Yang, AB Kerr, WH Tang, CH Meyer, A Macovski, JM Pauly, DG Nishimura, and BS Hu, "Rapid evaluation of left ventricular volume and mass without breath-holding using real-time interactive cardiac magnetic resonance imaging system", *J Am Col Cardiol*, vol. 38, no. 2, pp. 527-533, 2001

[13] KS Nayak, CH Cunningham, JM Santos, and JM Pauly, "Real-time cardiac MRI at 3 tesla", *Magn Reson Med*, vol. 51, no. 4, pp. 655-660, 2004

[14] HY Carr, "Steady-state free precession in nuclear magnetic resonance", *Phys Rev*, vol. 112, no. 5, pp. 1693-1701, 1958;

[15] K Scheffler, and S Lehnhardt, "Principles and applications of balanced SSFP techniques", *Eur Radiol*, vol. 13, no. 11, pp. 2409-2418, 2003

[16] KS Nayak, BA Hargreaves, BS Hu, DG Nishimura, JM Pauly, and CH Meyer, "Spiral balanced steady-state free precession cardiac imaging", *Magn Reson Med*, vol. 53, no. 6, pp. 1468-1473, 2005

[17] B Kressler, P Spincemaille, TD Nguyen, L Cheng, Z Xi Hai, MR Prince, and Y Wang, "Three-dimensional cine imaging using variable-density spiral trajectories and SSFP with application to coronary artery angiography", *Magn Reson Med*, vol. 58, no. 3, pp. 535-543, 2007

[18] KP Pruessmann, M Weiger, MB Scheidegger, and P Boesiger, "SENSE: sensitivity encoding for fast MRI", *Magn Reson Med*, vol. 42, no. 5, pp. 952-962, 1999

[19] MA Griswold, PM Jakob, RM Heidemann, M Nittka, V Jellus, J Wang, B Kiefer, and A Haase, "Generalized autocalibrating partially parallel acquisitions (GRAPPA)", *Magn Reson Med*, vol. 47, no. 6, pp. 1202-1210, 2002

[20] U Sumbul, JM Santos, and JM Pauly, "Improved time series reconstruction for dynamic magnetic resonance imaging", *IEEE Trans Med Imaging*, vol. 28, no. 7, pp. 1093-1104, 2009

[21] U Sumbul, JM Santos, and JM Pauly, "A practical acceleration algorithm for real-time imaging", *IEEE Trans Med Imaging*, vol. 28, no. 12, pp. 2042-2051, 2009

[22] A Macovski, "Volumetric NMR imaging with time-varying gradients", *Magn Reson Med*, vol. 2, no. 1, pp. 29-40, 1985

[23] E Adalsteinsson, J Star-Lack, CH Meyer, and DM Spielman, "Reduced spatial side lobes in chemical-shift imaging", *Magn Reson Med*, vol. 42, no. 2, pp. 314-323, 1999

[24] CM Tsai, and DG Nishimura, "Reduced aliasing artifacts using variable-density k-space sampling trajectories", *Magn Reson Med*, vol. 43, no. 3, pp. 452-458, 2000

[25] P Irarrazabal, CH Meyer, DG Nishimura, and A Macovski, "Inhomogeneity correction using an estimated linear field map", *Magn Reson Med*, vol. 35, no. 2, pp. 278-282, 1996

[26] DC Noll, JM Pauly, CH Meyer, DG Nishimura, and A Macovski, "Deblurring for non-2D Fourier transform magnetic resonance imaging", *Magn Reson Med*, vol. 25, no. 2, pp. 319-333, 1992

[27] W Chen, and CH Meyer, "Semiautomatic off-resonance correction in spiral imaging", *Magn Reson Med*, vol. 59, no. 5, pp. 1212-1219, 2008

[28] KF King, A Ganin, XJ Zhou, and MA Bernstein, "Concomitant gradient field effects in spiral scans", *Magn Reson Med*, vol. 41, no. 1, pp. 103-112, 1999

[29] W Chen, CT Sica and CH Meyer, "Fast conjugate phase image reconstruction based on a Chebyshev approximation to correct for B0 field inhomogeneity and concomitant gradients", *Magn Reson Med*, vol. 60, no. 5, pp. 1104-1111, 2008

[30] MA Bernstein, KF King, and XJ Zhou, "Handbook of MRI Pulse Sequence", *Elsevier academic press*, pp. 316-330, 2004

[31] X Feng, SW Fielden, H Tan, and CH Meyer, "K-space trajectory correction in spiral-in/out bSSFP imaging", in *Proc. 19th Ann. Meeting of ISMRM*, Montreal, Canada, p. 2457, 2011

[32] JH Duyn, Y Yang, JA Frank, and JW van der Veen, "Simple correction method for k-space trajectory deviations in MRI", *J Magn Reson*, vol. 132, no. 1, pp. 150-153, 1998

[33] H Tan, and CH Meyer, "Estimation of k-space trajectories in spiral MRI", *Magn Reson Med*, vol. 61, no. 6, pp. 1396-1404, 2009

[34] M Markl, and NJ Pelc, "On flow effects in balanced steady-state free precession imaging: pictorial description, parameter dependence, and clinical implications", *J Magn Reson Imaging*, vol. 20, no. 4, pp. 697-705, 2004

[35] T Parrish, and X Hu, "Continuous update with random encoding (CURE): a new strategy for dynamic imaging", *Magn Reson Med*, vol. 33, no. 3, pp. 326-336, 1995

[36] VS Deshpande, SM Shea, and D Li, "Artifact reduction in true-FISP imaging of the coronary arteries by adjusting imaging frequency", *Magn Reson Med*, vol. 49, no. 5, pp. 803-809, 2003

[37] CH Meyer, JM Pauly, A MAcovski, and DG Nishimura, "Simultaneous spatial and spectral selective excitation", *Magn Reson Med*, vol. 15, no. 2, pp. 287-304, 1990

[38] F Schick, "Simultaneously highly selective MR water and fat imaging using a simple new type of spectral-spatial excitation", *Magn Reson Med*, vol. 40, no. 2, pp. 194-202, 1998

[39] BA Hargreaves, SS Vasanawala, KS Nayak, BS Hu, and DG Nishimura, "Fat-suppressed steady-state free precession imaging using phase detection", *Magn Reson Med*, vol. 50, no. 1, pp. 210-213, 2003

[40] DP Kuehn, SL Ettema, MS Goldwasser, JC Barkmeier, and JM Wachtel, "Magnetic resonance imaging in the evaluation of occult submucous cleft palate", *Cleft Palate Craniofac J.*, vol. 38, no. 5, pp. 421-431, 2001

[41] A Serrurier, and P Badin, "A three-dimensional articulatory model of the velum and nasopharyngeal wall based on MRI and CT data", *J Acoust Soc Am*, vol. 123, no. 4, pp. 2335-2455, 2008

[42] BP Sutton, C Conway, Y Bae, C Brinegar, ZP Liang, and DP Kuehn, "Dynamic imaging of speech and swallowing with MRI", *Conf Proc IEEE Eng Med Biol Soc*, vol. 2009, no. 1, pp. 6651-6654, 2009

[43] M Fu, AG Christodoulou, AT Naber, DP Kuehn, ZP Liang, and BP Sutton, "High-frame-rate Multislice Speech Imaging with Sparse Sampling of (k,t)-space", in *Proc. 20th Ann. Meeting of ISMRM*, Melbourne, Australia, p. 12, 2012

[44] YC Kim, SS Narayanan, and KS Nayak, "Flexible retrospective selection of temporal resolution in real-time speech MRI using a golden-ratio spiral view order", *Magn Reson Med*, vol. 65, no. 5, pp. 1365-1371, 2011

[45] A Niebergall, S Zhang, E Kunay, G Keydana, M Job, M Uecker, and J Frahm, "Real-time MRI of speaking at a resolution of 33 ms: Undersampled radial FLASH with nonlinear inverse reconstruction", *Magn Reson Med*, Early View, 2012

[46] KP Pruessmann, M Weiger, P Bornet, and P Boesiger, "Advances in sensitivity encoding with arbitrary k-space trajectories", *Magn Reson Med*, vol. 46, no. 4, pp. 638-651, 2001

[47] M Lustig, and JM Pauly, "SPIRiT: Iterative self-consistent parallel imaging reconstruction from arbitrary k-space", *Magn Reson Med*, vol. 64, no. 2, pp. 457-471, 2010

[48] JA Fessler, and BP Sutton, "Nonuniform fast Fourier transforms using min-max interpolation", *IEEE Trans on Signal Processing*, vol. 51, no. 2, pp. 560-574, 2003

[49] DK Sodickson, and WJ Manning, "Simultaneous acquisition of spatial harmonics (SMASH): fast imaging with radiofrequency coil arrays", *Magn Reson Med*, vol. 38, no. 4, pp. 591-603, 1997

[50] WG Rehwald, RJ Kim, OP Simonetti, G Laub, and RM Judd, "Theory of high-speed MR imaging of the human heart with the selective line acquisition mode", *Radiology*, vol. 220, no. 2, pp. 540-547, 2001

[51] DL Donoho, "Compressed Sensing", *IEEE Trans Information Theory*, vol. 52, no. 4, pp. 1289-1306, 2006

[52] M Lustig, DL Donoho, and JM Pauly, "Sparse MRI: The application of compressed sensing for rapid MR imaging", *Magn Reson Med*, vol. 58, no. 6, pp. 1182-1195, 2007

[53] H Wang, D Liang, and L Ying, "Pseudo 2D random sampling for compressed sensing MRI", *Conf Proc IEEE Eng Med Biol Soc*, vol. 2009, pp. 2672-2675, 2009

[54] JP Haldar, D Hernando, and ZP Liang, "Compressed-sensing MRI with random encoding", *IEEE Trans Med Imaging*, vol. 30, no. 4, pp. 893-903, 2011

[55] Y Ding, YC Chung, M Jekic, and OP Simonetti, "A new approach to autocalibrated dynamic parallel imaging based on the Karhunen-Loeve transform, KL-TSENSE and KL-TGRAPPA", *Magn Reson Med*, vol. 65, no. 6, pp. 1786-1792, 2011

[56] SG Lingala, Y Hu, E DiBella, and M Jacob, "Accelerated dynamic MRI exploiting sparsity and low-rank structure: k-t SLR"', *IEEE Trans Med Imaging*, vol. 30, no. 5, pp. 1042-1054, 2011

[57] B Madore, GH Glover, and NJ Pelc, "Unaliasing by fourier-encoding the overlaps using the temporal dimension (UNFOLD), applied to cardiac imaging and fMRI", *Magn Reson Med*, vol. 42, no. 5, pp. 813-828, 1999

[58] J Tsao, P Boesiger, and KP Pruessmann, "k-t BLAST and k-t SENSE: dynamic MRI with high frame rate exploiting spatiotemporal correlations", *Magn Reson Med*, vol. 50, no. 5, pp. 1031-1042, 2003

[59] H Jung, K Sung, KS Nayak, EY Kim, and JC Ye, "k-t FOCUSS: a general compressed sensing framework for high resolution dynamic MRI", *Magn Reson Med*, vol. 61, no. 1, pp. 103-116, 2008

[60] X Hu, and T Parrish, "Reduction of field of view for dynamic imaging", *Magn Reson Med*, vol. 31, no. 6, pp. 691-694, 1994

[61] B Madore, JO Fredrickson, MT Alley, and NJ Pelc, "A reduced field-of-view method to increase temporal resolution or reduce scan time in cine MRI", *Magn Reson Med*, vol. 43, no. 4, pp. 549-558, 2000

[62] ME Brummer, D Moratal-Perez, CY Hong, RI Pettigrew, J Millet-Roig, and WT Dixon, "Noquist: reduced field-of-view imaging by direct Fourier inversion", *Magn Reson Med*, vol. 51, no. 2, pp. 331-342, 2004

[63] EV Di Bella, YJ Wu, AL Alexander, DL Parker, D Green, and CJ McGann, "Comparison of temporal filtering methods for dynamic contrast MRI myocardial perfusion studies", *Magn Reson Med*, vol. 49, no. 5, pp 895-902, 2003

[64] G Adluru, SP Awate, T Tasdizen, RT Whitaker, and EV Dibella, "Temporally constrained reconstruction of dynamic cardiac perfusion MRI", *Magn Reson Med*, vol. 57, no. 6, pp. 1027-1036, 2007

[65] P Kellman, FH Epstein, and ER McVeigh, "Adaptive sensitivity encoding incorporating temporal filtering (TSENSE)", *Magn Reson Med*, vol. 45, no. 5, pp. 846-852, 2001

[66] FA Breuer, P Kellman, MA Grisswold, and PM Jakob, "Dynamic autocalibrated parallel imaging using temporal GRAPPA (TGRAPPA)", *Magn Reson Med*, vol. 53, no. 4, pp. 981-985

[67] LH Hamilton, JA Fabregat, D Moratal, S Ramamurthy, S Lerakis, WJ Parks, D Sallee, and ME Brummer, ""PINOT": time-resolved parallel magnetic resonance imaging with a reduced dynamic field of view", *Magn Reson Med*, vol. 65, no. 4, pp. 1062-1074, 2011

[68] WE Kyriakos, LP Panych, DF Kacher, CF Westin, SM Bao, RV Mulkern, and FA Jolesz, "Sensitivity profiles from an array of coils for encoding and reconstruction in parallel (SPACE RIP)", *Magn Reson Med*, vol. 44, no. 2, pp. 301-308, 2000

[69] Analytic Sciences Corporation. Technical Staff., A Gelb, "Applied optimal estimation", *Cambridge, Mass.,: M.I.T. Press*, 1974

[70] M Buehrer, KP Pruessmann, P Boesiger, and S Kozerke, "Array compression for MRI with large coil arrays", *Magn Reson Med*, vol. 57, no. 6, pp. 1131-1139, 2007